Dynamics of two episodes of high winds produced by an unusually long-lived quasi-linear convective system in South China

Xin Xu[1,2,*], Yuanyuan Ju[1,2], Qiqing Liu[1,2], Kun Zhao[1,2], Ming Xue[1,3], Shushi Zhang[4], Ang Zhou[1,2], Yuan Wang[1], Ying Tang[5]

[1]*Key Laboratory of Mesoscale Severe Weather/Ministry of Education, and School of Atmospheric Sciences, Nanjing University, Nanjing 210023, Jiangsu, China*

[2]*Key Laboratory of Radar Meteorology, China Meteorology Administration, Nanjing 210023, Jiangsu, China*

[3]*Center for Analysis and Prediction of Storms, University of Oklahoma, Norman 73072, OK, US*

[4]*Key Laboratory of Transportation Meteorology of China Meteorological Administration, Nanjing Joint Institute for Atmospheric Sciences, Nanjing 210000, Jiangsu, China*

[5]*Nanjing Marine Radar Institute, Nanjing 210000, Jiangsu, China*

Submitted to *Journal of the Atmospheric Sciences*

14 March 2023

Corresponding author: Xin Xu, xinxu@nju.edu.cn

Early Online Release: This preliminary version has been accepted for publication in *Journal of the Atmospheric Sciences*, may be fully cited, and has been assigned DOI 10.1175/JAS-D-23-0047.1. The final typeset copyedited article will replace the EOR at the above DOI when it is published.

ABSTRACT

Using radar observation and convection-permitting simulation, this work studies the storm-scale dynamics governing the generation of two episodes of high winds by an unusually long-lived quasi-linear convective system (QLCS) in South China on 21 April 2017. The first episode of high winds occurred at the apex of a bowing segment in the southern QLCS due to the downward transport of high momentum by a descending rear-inflow jet (RIJ). The RIJ was initially elevated, generated as low-frequency gravity wave response to the thermal forcing in the QLCS leading convective line. It descended to the surface owing to the enhancement of low-level diabatic cooling which strengthened the downdrafts at the RIJ leading edge. Vertical momentum budget revealed that the downdrafts were initiated by the negative buoyancy of cold pool and strengthened by the weakened buoyancy-induced upward pressure gradient force in the boundary layer and enhanced hydrometeor loading above. The second episode of high winds occurred in the decaying stage of the QLCS which, however, redeveloped as its northern part interacted with an intensifying large-scale shear line to the east. A zonal convective line developed along the shear line and finally merged with the QLCS. The merger greatly enhanced the low-level convergence, leading to downward development of the line-end vortex via vertical stretching of vertical vorticity. The area of high winds was notably increased by the superposition of the ambient translational wind with the vortex rotational flow. The findings provide new insights into the generation of high winds by QLCS-MCS merger, highlighting the importance of low-level vortices in addition to the RIJ.

Accepted for publication in *Journal of the Atmospheric Sciences*. DOI 10.1175/JAS-D-23-0047.1.

SIGNIFICANCE STATEMENT

Quasi-linear convective systems (QLCSs) are prolific producers of high winds at the surface. While conceptual models have been established for high winds produced by single QLCSs, this is not the case for the high winds generated by QLCSs merging with other convective systems. This work revealed different dynamics for two episodes of high winds produced by a long-lived QLCS merging with an MCS in South China. The first episode resulted from the descending rear-inflow jet (RIJ) as in the case of single QLCSs. The second and stronger one was due to the superposition of ambient flow with a line-end vortex that developed downward given the enhanced low-level convergence by the merger. This finding sheds lights on the importance of mergers in high-wind generation which has even greater damaging potential than the RIJ.

Accepted for publication in *Journal of the Atmospheric Sciences*. DOI 10.1175/JAS-D-23-0047.1.

1. Introduction

Quasi-linear convective systems (QLCSs), e.g., squall lines and bow echoes, are known to produce high winds at the surface which can reach the intensity of tornadoes (e.g., Weisman 2001). Unlike tornadoes, QLCSs generally produce a straight-line swath of high winds which can be up to hundreds of kilometers long and tens of kilometers wide, i.e., derecho (Johns and Hirt 1987). For example, the 8 May 2009 Super Derecho, which was one of the most intense and unusual derechos ever observed in the United States, produced severe wind gusts in excess of 50 m s^{-1} (e.g., Coniglio et al. 2011; Xu et al. 2015a). Travelling more than 1000 miles in 24 hours, this high wind-producing convective system caused widespread fallen trees and power lines, leading to economic loss of about $115 million (Evans et al. 2014).

Many efforts have been made in the past few decades to explore the mechanisms of high winds produced by QLCSs given their damaging potential. Early observational and numerical studies (e.g., Fujita 1978; Smull and Houze 1987; Lafore and Moncrieff 1989; Weisman 1992) found that the mid-level rear-inflow jet (RIJ) that feeds into the stratiform region of QLCSs plays an important role in producing the high winds at the surface. Fundamentally, the RIJ can be viewed as a gravity wave response to the mean heating in the convective line and stratiform region (e.g., Pandya and Durran 1996; Pandya et al. 2000; Fovell 2002). The mid-level negative pressure perturbations caused by the vertical gradient of buoyancy between the upshear-tilted convective updrafts and the surface cold pool can help enhance the RIJ. Moreover, the counter-rotating bookend vortices that form at the two ends of the QLCSs also have an important contribution to the RIJ (Weisman and Davis 1998). The RIJ supplies potentially cold and dry air into the QLCSs, which aids in the production of convective downdrafts. Once the RIJ descends to the ground, near-surface high winds are generated via downward transport of momentum (Mahoney and Lackmann 2011). The descent of the RIJ is usually attributed to the latent cooling by sublimation, melting and evaporation of precipitation particles as well as hydrometeor loading (e.g., Zhang and Gao 1989; Yang and Houze 1995; Houze 2004; Mahoney and Lackmann 2011; Adams-Selin and Johnson 2013;

Accepted for publication in *Journal of the Atmospheric Sciences*. DOI 10.1175/JAS-D-23-0047.1.

Zhou et al. 2020). Based upon the budgets of vertical momentum for the RIJ of the 8 May 2009 Super Derecho, Xu et al. (2015b) found that the blocking of the RIJ by the leading-edge convective updrafts can induce a downward-directed dynamic pressure gradient force which contributes to the descent of the RIJ as well.

A field campaign, namely, bow echo and mesoscale convective vortex experiment (BAMEX), was carried out between 20 May and 6 July 2003 over the central United States by using a variety of mobile platforms (Davis et al. 2004). One of the scientific objectives of BAMEX is to improve the understanding and prediction of high winds produced by QLCSs, especially bow echoes. Radar and damage survey analyses of the bow echoes observed during BAMEX showed that the primary straight-line wind swath may be not collocated with the bow apex where the RIJ is often present, but with the low-level meso-γ-scale vortices (MVs) formed on the leading edge of the bow echoes (Atkins et al. 2005; Wheatley et al. 2006). This provided observational evidences for the idealized numerical simulations of QLCSs conducted by Weisman and Trapp (2003) which found that MVs may be responsible for the production of damaging straight-line winds. MVs can notably modify the local outflow and determine the location of wind speed maxima. The strongest winds tend to occur on the side of the MV where the ambient translational flow and the MV rotational flow are in the same direction (e.g., Wakimoto et al. 2006; Atkins and Laurent 2009; Xu et al. 2015b).

Previous studies mainly focused on the high winds produced by single QLCSs. In reality, however, QLCSs may merge with other convective systems during evolution. For instance, thunderstorm mergers were found in association with the formation of bow echoes 50%–55% of the time according to radar observations of 273 bow echoes over the United States during the period of 1996-2002 (Klimowski et al. 2004). Using radar observations and severe storm reports in the warm season of 2006–2010, French and Parker (2012) documented 21 cases of squall line-supercell merger over the central United States. They found that the severe wind reports tended to maximize after the merger, suggesting a connection between the merger and high winds. Based on a series of idealized numerical simulations, French and Parker (2014) examined the storm-scale processes responsible for the evolution of squall line merged with isolated supercell.

Accepted for publication in *Journal of the Atmospheric Sciences*. DOI 10.1175/JAS-D-23-0047.1.

The merger can promote a more compact bowing segment by locally strengthening the cold pool and RIJ, thus representing a favored location for severe weather production relative to other parts of the squall line.

QLCSs in China have also received great interest. Using 2-yr radar and rawinsonde observations, Meng et al. (2013) examined the general features of squall lines in East China, e.g., spatiotemporal characteristics, formation and organization modes, and ambient conditions. Squall lines in China are generally formed in a moister environment with comparable background instability but weaker vertical shear than those in the United States. Yang et al. (2017) studied the 5-yr climatology of severe convective winds in China which most frequently occurred in Guangdong province, South China in spring. Chen et al. (2022) also found a high occurrence frequency of derechos in South China during 2002–2019. These are in line with the high occurrence frequency of squall lines in South China (Meng et al. 2013). Xue et al. (2022) investigated the organization modes of the spring and summer convective storms and associated severe weather in South China during 2015–2019. Bow echoes and linear convective systems with parallel stratiform precipitation were identified to be the main producers of severe wind events.

Besides climatology studies, there are also case studies exploring the formation of QLCSs and associated high winds in China (e.g., Yao et al. 2008; Sun et al. 2011; Meng et al. 2012; Xia et al. 2012; Quan et al. 2014; Abulikemu et al. 2015; Zhang et al. 2021; Liu et al. 2023). Most of these studies were observation-based (e.g., radar, satellite, sounding) analyses which basically addressed single QLCSs without merger with other convective systems. Using 5-yr radar observations, Zhou et al. (2023) found that merger-formation bow echoes (MFBEs) can account for more than half of the total bow echoes in South China. In this regard, more studies are needed to improve the understanding of merger-type QLCSs and associated severe weather (e.g., damaging surface winds, heavy rainfall) in China. Zhou et al. (2020) studied a MFBE in South China using polarimetric radar observation and the analyses of the variational Doppler radar analysis system (VDRAS) (Sun and Crook 2001). Although the cold pool and RIJ were enhanced by the merger as in the idealized simulations of French and Parker

Accepted for publication in *Journal of the Atmospheric Sciences*. DOI 10.1175/JAS-D-23-0047.1.

(2014), there were no appreciable high winds produced at the surface in this case. Hence, the mechanisms of damaging surface winds produced by merger-type QLCSs in China still remains poorly understood.

On 21 April 2017, there occurred a long-lived QLCS in South China which lasted for more than 15 hours. For reference, about 95% of linear convective systems in South China are shorter than 15 hours, with a mean lifetime of 7.3 hours in spring (Xue et al. 2022). During this long-lasting QLCS event, there were a number of high wind ($\geq$ 17.2 m s^{-1}) reports, with the most severe wind (32.4 m s^{-1}) observed after the QLCS merged with another mesoscale convective system (MCS) to its east. The main purpose of this research is to explore the storm-scale dynamics responsible for the high winds produced by this unusually long-lived QLCS using a convection-permitting numerical simulation. In particular, what is the role of the merger in enhancing the high winds at the surface? The rest of this manuscript is structured as follows. Section 2 describes the datasets used in this work and the setup of numerical experiment. Section 3 presents the ambient conditions of the QLCS and its evolution and associated high winds. The generation mechanisms of high winds produced by this merger-type QLCS are examined in section 4. Section 5 summarizes the key findings with discussions.

2. Data and method

2.1 Datasets

The evolution of the QLCS under consideration is studied using the observations of four *S*-band operational Doppler radars in Guangdong province, South China (see their locations in Fig. 1a), i.e., Guangzhou (9200), Yangjiang (9662), Shaoguan (9751), and Shantou (9754), with a time interval of 6 minutes. A procedure of quality control, e.g., noise and ground clutter removal, despeckling and velocity dealiasing (Brewster et al. 2005), is applied to the raw radar data using the 88D2ARPS program of Advanced Regional Prediction System (Xue et al. 2000) developed at the Center for Analysis and Prediction of Storms (CAPS), University of Oklahoma. This program was used in our previous studies (e.g., Hua et al. 2020; Tang et al. 2020; Tang et al. 2022) which can

Accepted for publication in *Journal of the Atmospheric Sciences*. DOI 10.1175/JAS-D-23-0047.1.

effectively eliminate non-meteorological echoes and make radial velocity unfolded. For the damaging winds produced by the QLCS, the operational severe weather reports are adopted which record high winds of ≥ 17.2 m s^{-1}. The environment conditions of the QLCS are studied using the hourly, 0.25°×0.25° fifth generation of the European Centre for Medium-Range Weather Forecasts (ECMWF) atmospheric reanalysis of the global climate (ERA5) (Hersbach et al. 2020). An upper air sounding at Hongkong (see its location in Fig. 1a) is also utilized.

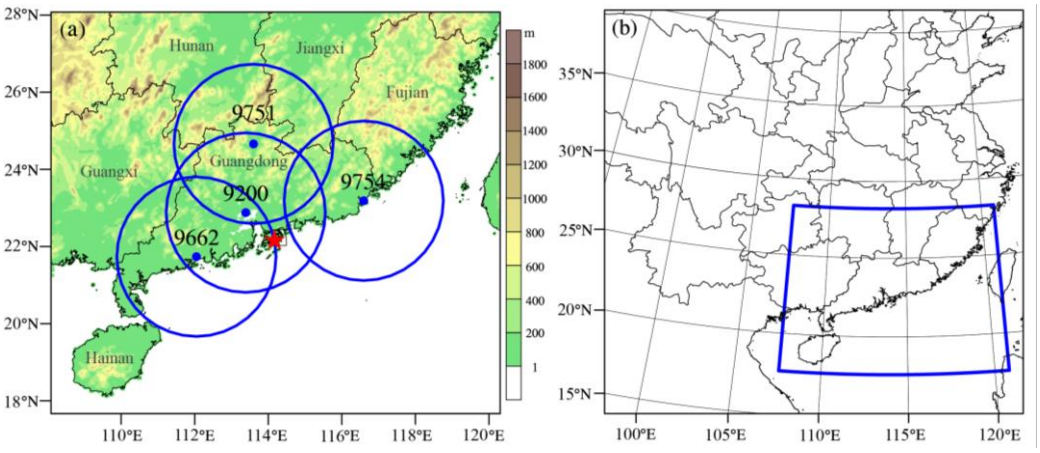

Fig.1 (a) Terrain (shading, unit: m) in South China. The blue dots indicate the locations of the four operational radars including Guangzhou (9200), Yangjiang (9662), Shaoguan (9751) and Shantou (9754). The blue circles represent the 230-km range for each radar. The red star marks the location of atmospheric sounding in Hongkong. (b) Domain of the WRF model. The blue box denotes the region of (a).

2.2 Setup of numerical experiment

A convection-permitting numerical simulation is conducted using the Advanced Research version of the Weather Research and Forecasting (WRF) model (Skamarock et al. 2019). The model is configured with a single domain of 685×742 grid points, with a horizontal resolution of 4 km (Fig. 1b). In the vertical, there are 50 levels from surface to the 50-hPa model top. For the model physics, we adopt the Thompson microphysics scheme (Thompson et al. 2008), the Mellor–Yamada–Janjic (MYJ) planetary boundary layer (PBL) scheme (Janjić 1994), the Goddard and RRTMG schemes for shortwave and longwave radiation respectively (Matsui et al. 2020; Iacono et al. 2008), the Eta

Accepted for publication in *Journal of the Atmospheric Sciences*. DOI 10.1175/JAS-D-23-0047.1.

Similarity scheme for surface layer, and the Unified Noah land surface model(Tewari et al. 2004). No parameterization scheme is used for cumulus convection given the 4-km grid spacing. The simulation starts at 1200 UTC on 20 April 2017 and is integrated for 24 hours, with a timestep of 20 seconds. The model initial and boundary conditions are derived from the ERA5 reanalysis.

3. Case Overview

3.1 Environment conditions

As shown in Fig. 2a, there was a 500-hPa short-wave trough in North China, while the QLCS developed in South China where the synoptic forcing was weak in the middle troposphere. Nevertheless, South China was just located on the right entrance region of an exceptionally strong upper-level jet max (> 70 m s^{-1}) where deep, moist convection are favored by the upward motion of the cross-jet secondary circulation. At 850 hPa (Fig. 2b), there was a shear line in South China, with northeasterlies and southwesterlies to the north and south of about 22°N, respectively. This shear lines formed as the mid-latitude westerlies were blocked by the Tibetan Plateau and splitted into two branches that detoured the plateau, which finally re-converged in the downstream region of the plateau (Wu et al. 2015). The low-level southwesterly flow transported warm, moist air of high equivalent potential temperature (θ_e) from the South China Sea and the Bay of Bengal, which moistened the lower troposphere and increased the thermal instability in South China. The QLCS just developed along the low-level shear line near the core of the high-θ_e tongue at (110°E, 22°N). Note that the northern portion of the convective system interacted with the 850 hPa shear line, while the southern portion and bow echo did not.

Accepted for publication in *Journal of the Atmospheric Sciences.* DOI 10.1175/JAS-D-23-0047.1.

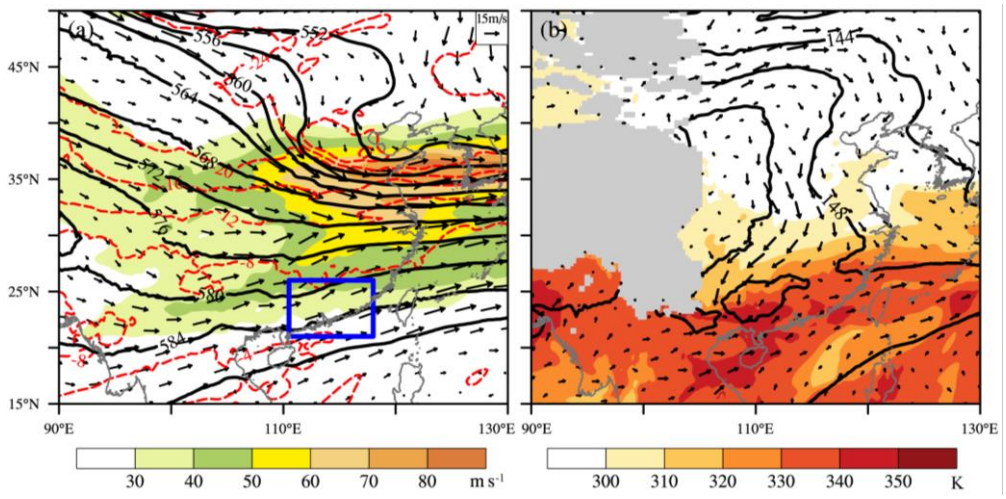

Fig. 2 (a) The geopotential height (black solid contours; unit: 10 gpm), temperature (red dashed contours; unit: ℃) and horizontal winds (vectors) at 500 hPa and horizontal wind speed (shading; unit: m s^{-1}) at 200 hPa at 0000 UTC on 21 April 2017. (b) Same as (a) but for the geopotential height (contours; unit: 10 gpm), horizontal wind (vectors), and equivalent potential temperature (shading; unit: K) at 850 hPa. The blue box in (a) indicates the region where the QLCS under consideration developed. The light gray line in (a) and (b) represents the national border of China.

The atmospheric sounding at Hongkong at 0000 UTC on 21 April showed that the lifted condensation level (LCL) was very low at 951 hPa, accompanied with a low level of free convection (LFC) at 922 hPa (Fig. 3a). By contrast, the atmosphere was rather dry above 850 hPa, presumably due to the dry intrusion from northwest. This unstable thermal structure led to a high convective available potential energy (CAPE) of 2294 J kg^{-1} and a weak convection inhibition (CIN) of -2.1 J kg^{-1}. The downward convective available potential energy (DCAPE) is 1028.3 J kg^{-1} which suggests a high potential for the occurrence of strong downdrafts. Due to the low-level warm advection, the horizontal winds in general veered with height below about 3 km (Fig. 3b). There was a moderate-to-strong vertical wind shear of 15 m s^{-1} (25 m s^{-1}) from the surface to 3 km (6 km), which was conductive to the development of organized QLCS.

Accepted for publication in *Journal of the Atmospheric Sciences*. DOI 10.1175/JAS-D-23-0047.1.

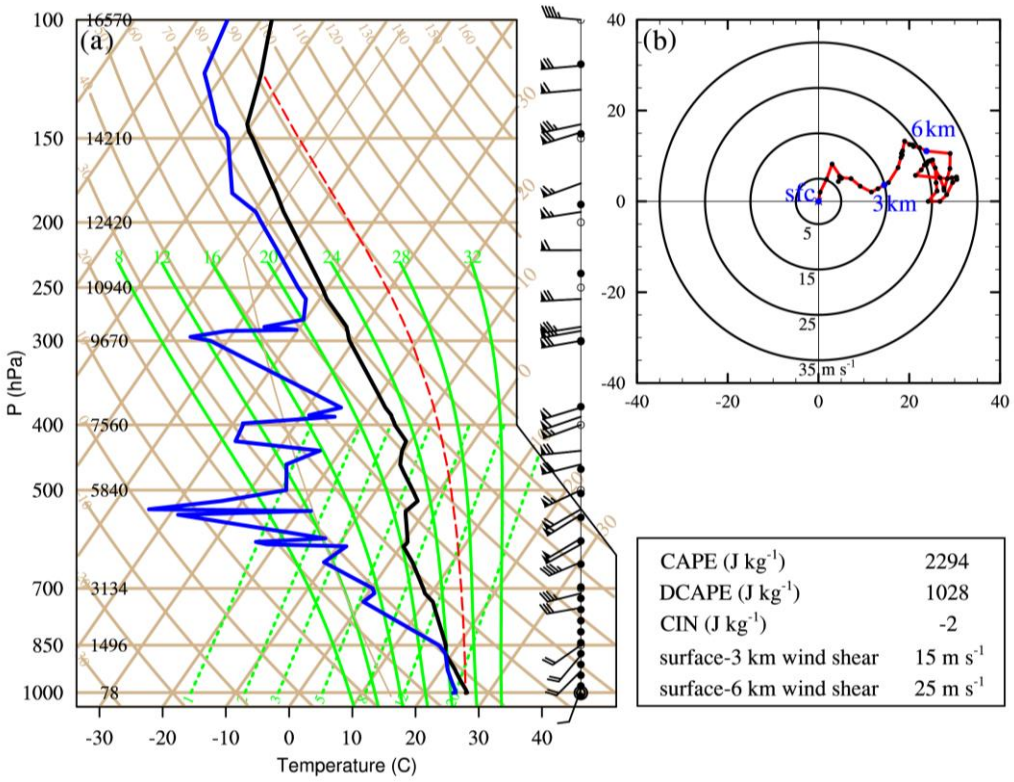

Fig. 3 (a) Atmospheric sounding and (b) hodograph observed at Hongkong (denoted by the red star in Fig. 1a) at 0000 UTC on 21 April 2017.

3.2 Evolution of the QLCS and associated high winds

Figure 4 shows the composite reflectivity (i.e., column maximum reflectivity) of the four operational *S*-band radars in Guangdong province from 0100 to 0800 UTC on 21 April 2017. At 0100 UTC (Fig. 4a) there were two MCSs. One was located in central-east Guangdong province which was the remnant of a decaying MCS that occurred on 20 April (not shown). The other was located at the border of Guangdong and Guangxi provinces, which finally caused the high winds of interest. While this MCS initiated in Guangxi province at an earlier time, we are unable to investigate its early evolution due to the limit of available radar coverage (Fig. 1a). In the next few hours (Figs. 4b-4d), the western MCS entered Guangdong province and developed into a QLCS, exhibiting a mixed feature of parallel stratiform (PS) and leading stratiform (LS) precipitation (Parker and Johnson 2000). The latter was attributed to the strong westerly vertical wind shear (Fig. 3b). As revealed in Xue et al. (2022), PS-type linear convective systems are abundant producers of springtime severe wind events in South China. A small bowing

Accepted for publication in *Journal of the Atmospheric Sciences*. DOI 10.1175/JAS-D-23-0047.1.

segment can be found at the southernmost end of the QLCS. At 0500 UTC (Fig. 4e), the QLCS evolved into a system-scale bow echo, with notable trailing stratiform (TS) precipitation. Meanwhile, the decaying MCS to the east of the bow echo experienced a redevelopment. The scattered convective cells observed in the western part of the decaying MCS at 0200 and 0300 UTC (Figs. 4b, 4c) organized into a small convective line to the immediate north of the Pearl River Delta region at 0500 UTC (Fig. 4e). The system-scale bow echo lasted about one hour and became a QLCS again at 0600 UTC when it caught up with the eastern MCS (Fig. 4f). That is, the two convective systems merged.

The merger is better shown in Fig. 5 which depicts the composite reflectivity in a zoomed-in area. At 0418 UTC (Fig. 5a), scattered convective cells were found between the QLCS and the decaying MCS, which organized into a quasi-continuous line at 0430 UTC (Fig. 5b). The intensity of this small line developed over time (Figs. 5c, 5d) and merged with the QLCS at 0512 UTC (Fig. 5e). Later at 0530 UTC, the decaying MCS merged with the small convective line and hence the bow echo (Fig. 5f). The convection was evidently enhanced in the merger region, as revealed by the expanded area of 30-dBZ (Fig. 4g). Finally, an elongated linear convective system formed along the coast of Guangdong province (Fig. 4h) which propagated southeastward to the South China Sea in the next few hours (not shown).

Accepted for publication in *Journal of the Atmospheric Sciences*. DOI 10.1175/JAS-D-23-0047.1.

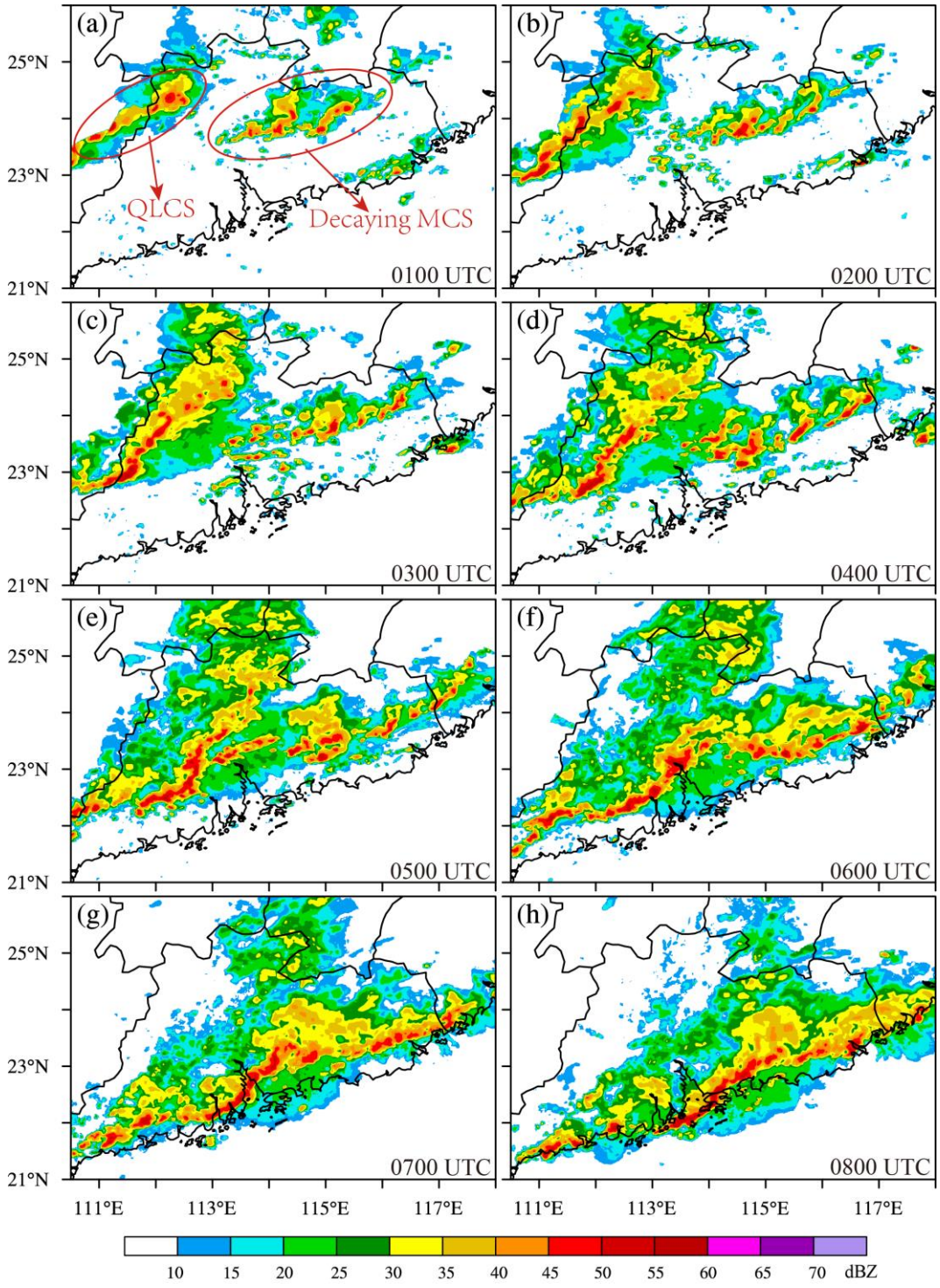

Fig. 4 Composite reflectivity (shading; unit: dBZ) of the four radars in Guangdong province at (a) 0100 UTC, (b) 0200 UTC, (c) 0300 UTC, (d) 0400 UTC, (e) 0500 UTC, (f) 0600 UTC, (g) 0700 UTC, and (h) 0800 UTC on 21 April 2017. The area shown here is the same as the blue box in Fig. 2a.

Accepted for publication in *Journal of the Atmospheric Sciences*. DOI 10.1175/JAS-D-23-0047.1.

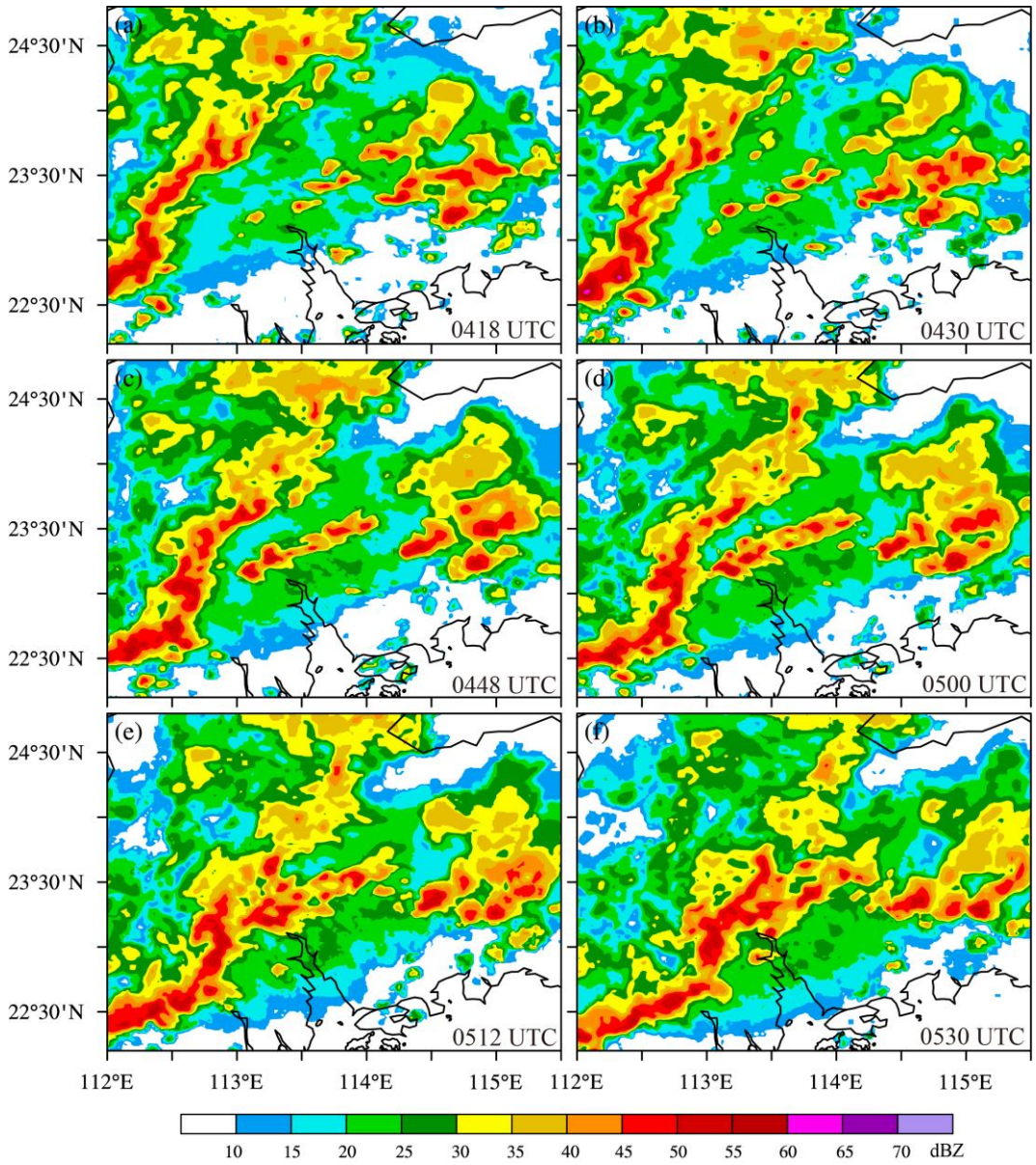

Fig. 5 Same as Fig. 4 but for the composite reflectivity (shading; unit: dBZ) in a zoomed-in area at (a) 0418 UTC, (b) 0430 UTC, (c) 0448 UTC, (d) 0500 UTC, (e) 0512 UTC, and (f) 0530 UTC on 21 April 2017.

During the evolution of this QLCS, a number of high winds were observed by automatic weather stations in Guangdong province from about 0300 to 1000 UTC (Fig. 6a). High winds mainly occurred in the central and northern parts of the QLCS between 0530 and 0700 UTC, i.e., during the merger of the system with the decaying MCS (Fig. 6b). In the early stage of 0300-0400 UTC (Fig. 7a), the observed high winds were associated with the southern bowing segment, with the wind speed generally less than 20 m s^{-1} (but $\geqslant$17.2 m s^{-1}). As the QLCS evolved into a system-scale bow echo at 0500

Accepted for publication in *Journal of the Atmospheric Sciences*. DOI 10.1175/JAS-D-23-0047.1.

UTC (Fig. 7b), high winds were mainly located at and behind the bow apex, which were stronger than at earlier time. As the QLCS merged with the eastern MCS at 0600 UTC (Fig. 7c), both the number and intensity of the observed high winds increased remarkably during this hour, with the most severe winds over 30 m s^{-1} occurring in the merger region. When the QLCS moved to the coastal line, there were much fewer high winds (Fig. 7d). While it is likely due to the decay of the system, the sparse observations over the sea may underestimate the number of high winds.

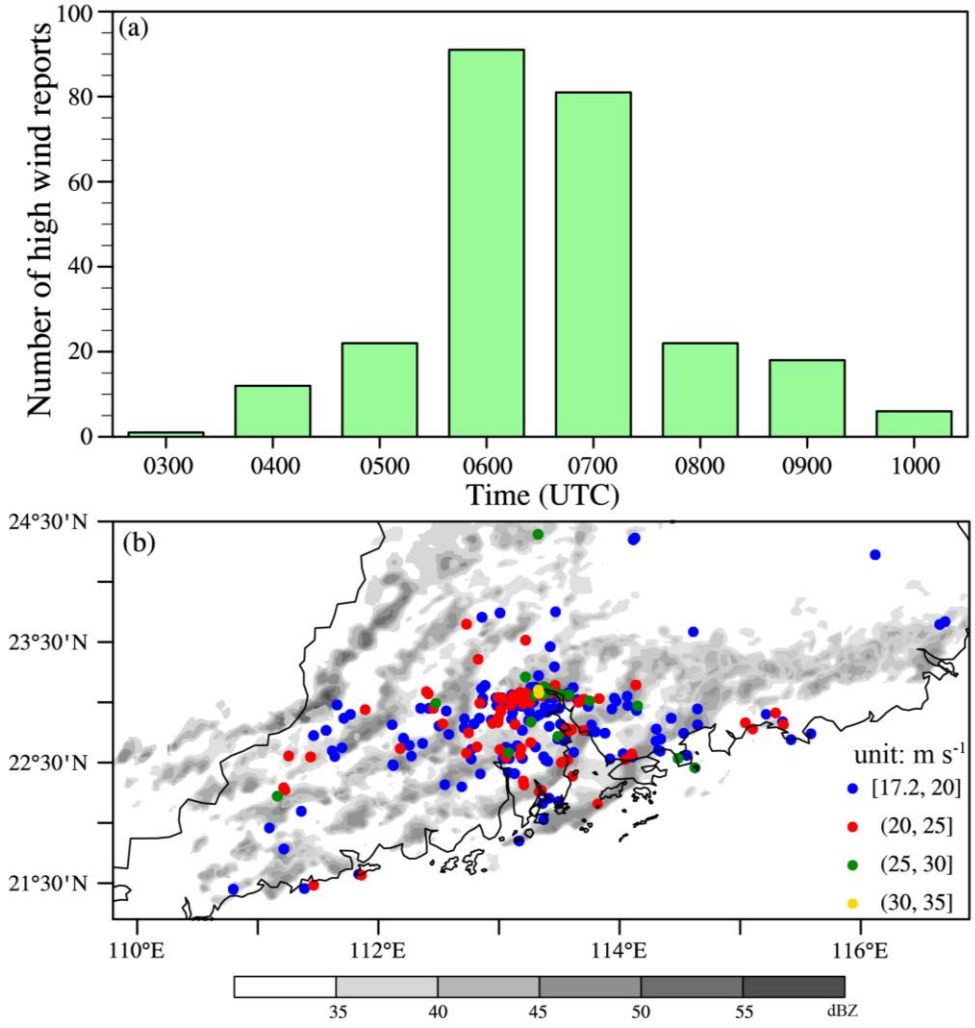

Fig. 6 (a) Accumulated number of high winds (≥17.2 m s^{-1}) reported within each hour. (b) High winds reported between 0300 and 0800 UTC on 21 April 2017. The grey shading designates the hourly composite reflectivity (unit: dBZ) from the four radars in Guangdong province.

Accepted for publication in *Journal of the Atmospheric Sciences*. DOI 10.1175/JAS-D-23-0047.1.

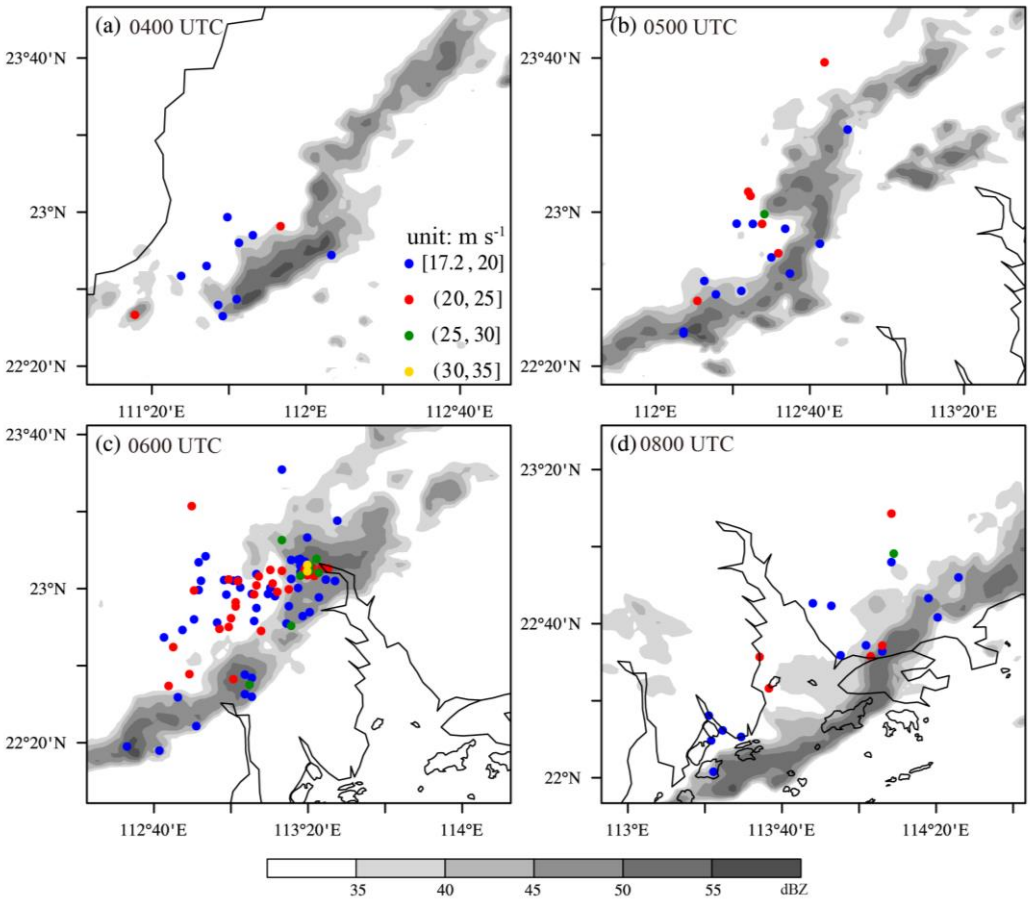

Fig. 7 The high wind reports during (a) 0300-0400 UTC, (b) 0400-0500 UTC, (c) 0500-0600 UTC and (d) 0700-0800 UTC on 21 April 2017. Gray shading is the composite reflectivity at 0400, 0500, 0600 and 0800, respectively.

4. Generation of high winds by the QLCS

4.1 Model verification

Figure 8 displays the composite reflectivity of the simulated QLCS. At 0330 UTC (Fig. 8a), the system reached the border of Guangdong and Guangxi provinces, showing a mixed feature of PS and LS precipitation as in observation. There occurred a bowing segment on its southern end as well. Half an hour later (Fig. 8b), the convective system showed a more apparent bow shape, with the maximum composite reflectivity reaching 60 dBZ. At 0418 UTC (Fig. 8c), scattered convective cells were found in the region between the QLCS and the decaying MCS to the east, which developed over time and organized into a west-east convective line at 0500 UTC (Figs. 8d, 8e), consistent with

Accepted for publication in *Journal of the Atmospheric Sciences*. DOI 10.1175/JAS-D-23-0047.1.

observation (see Fig. 5). At 0530 UTC (Fig. 8f), the leading convective line of the QLCS was about to catch up with the newly formed convective line to its east. The system lost its bow shape at 0600 UTC (Fig. 8g), because of the decay of convection in its central part. By contrast, a continuous development of convection was found in the northern part of the system where the merger occurred (Figs. 8g-8i). Finally, an elongated linear convective system formed along the coast of Guangdong province (Fig. 8j). Overall, the evolution of the QLCS was well captured by the WRF model, including the early bowing stage and the later merger, despite some timing and positioning biases which are common in real-data simulations of MCSs.

Figure 9 presents the evolution of the simulated horizontal wind speed at 100 m above ground level (AGL). [The horizontal wind speed at the lowest model level of ~30 m AGL is qualitatively similar to the 100-m wind speed (not shown).] The horizontal wind speed at 1500 m MSL is shown as well. At 0300 UTC (Fig. 9a), high winds of ≥ 17.2 m s^{-1} emerged at the apex of the bowing segment in the southern QLCS. In the next two hours (Figs. 9b-9e), the QLCS evolved into a system-scale bow echo; both the intensity and area of high winds were increased at the bow apex. At 0530 UTC (Fig. 9f), while the system still maintained its bowing structure, the high winds at the bow apex (more precisely, to the south of the bow apex) diminished. In contrast, high winds were found to develop in the northern part of the system where the system merged with the remnant MCS to its east. During the merger (Figs. 9g-9i), the intensity of high winds was significantly enhanced, with the strongest winds in excess of 30 m s^{-1}. The area of high winds also increased, much broader than in the early stage. The near-surface high winds weakened evidently and totally disappeared after 0800 UTC (not shown). From the above analyses, the near-surface high winds simulated by the WRF model share many similarities with observation in the aspects of timing, location and intensity. In the next subsections, the WRF model outputs are used to examine the mechanisms of high winds in different stages of the QLCS.

Accepted for publication in *Journal of the Atmospheric Sciences*. DOI 10.1175/JAS-D-23-0047.1.

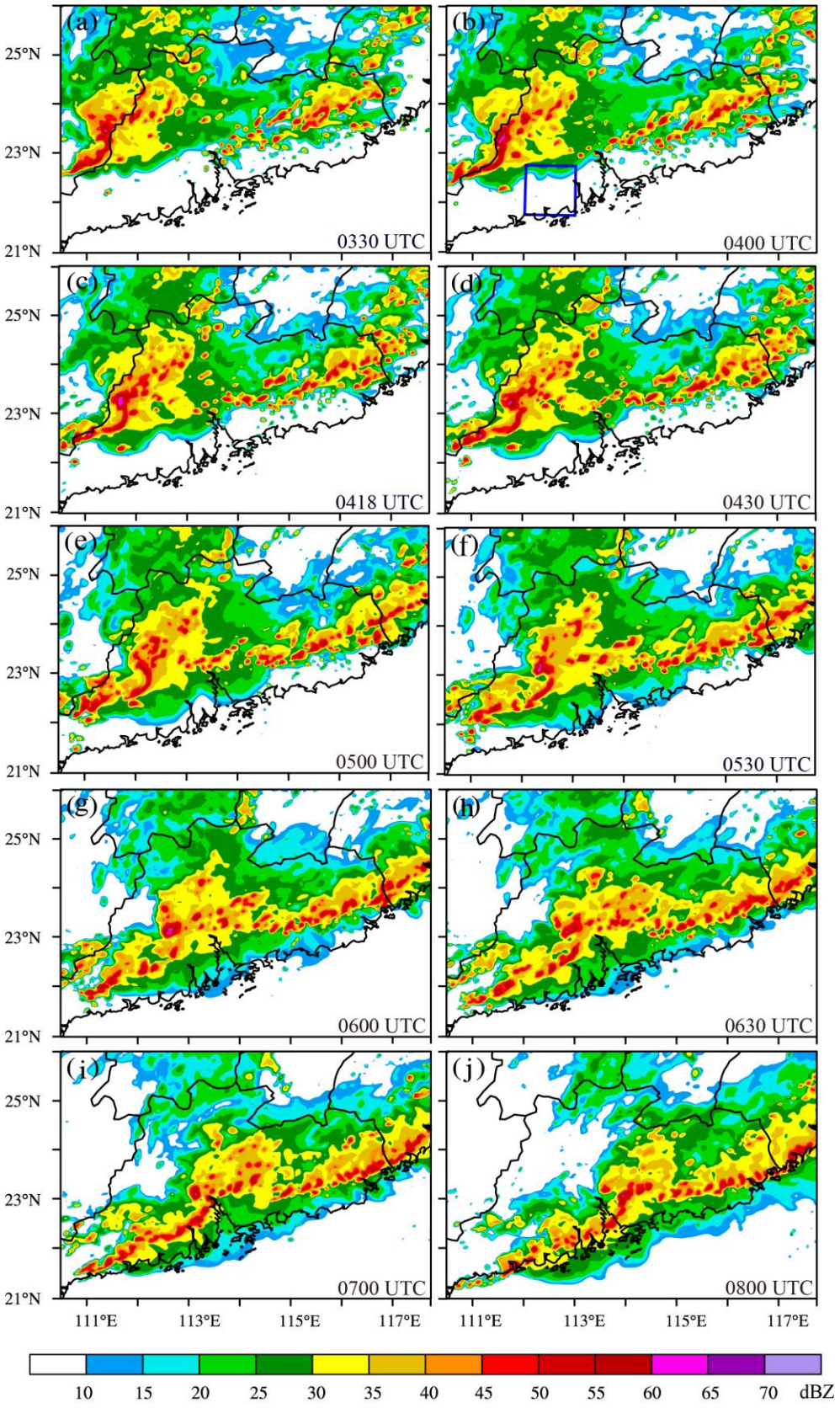

Fig. 8 Same as Fig. 4 but for the simulated composite reflectivity (shading; unit: dBZ) at (a) 0330 UTC, (b) 0400 UTC, (c) 0418 UTC, (d) 0430 UTC, (e) 0500 UTC, (f) 0530 UTC, (g) 0600 UTC, (h) 0630 UTC, (i) 0700 UTC and (j) 0800 UTC on 21 April 2017.

Accepted for publication in *Journal of the Atmospheric Sciences*. DOI 10.1175/JAS-D-23-0047.1.

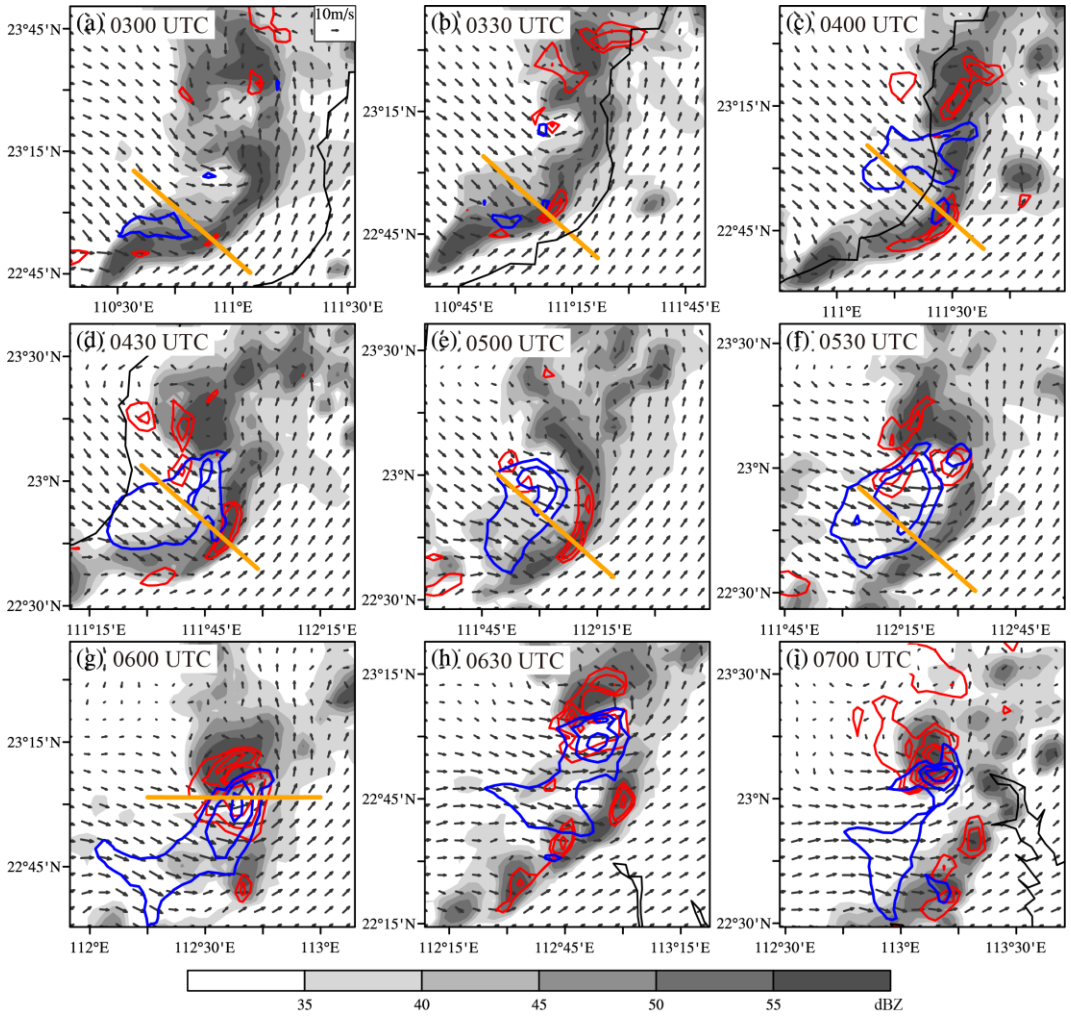

Fig. 9 Simulated horizontal wind (vectors) and speed (blue contours; unit: m s^{-1}) at 1500 m MSL, horizontal wind speed at 100 m AGL (red contours; unit: m s^{-1}), and composite reflectivity (shading; unit: dBZ) at (a) 0300 UTC, (b) 0330 UTC, (c) 0400 UTC, (d) 0430 UTC, (e) 0500 UTC, (f) 0530 UTC, (g) 0600 UTC, (h) 0630 UTC, and (i) 0700 UTC on 21 April 2017. Blue contours start from 25 m s^{-1} with an interval of 5 m s^{-1}, while red contours are 17.2 m s^{-1}, 20 m s^{-1}, 25 m s^{-1}, 30 m s^{-1} and 35 m s^{-1}, respectively. The orange lines in (a)-(f) and (g) denote the locations of vertical planes shown in Figs. 10 and 11 respectively.

4.2 High winds in the early stage

In the early stage, the high winds mainly occurred at the apex of the bowing segment in the southern QLCS. At 1.5 km MSL, prominent northwesterly flow protruded toward the bow apex (Fig. 9) which resembled the well-known RIJ. Pandya and Durran (1996) found that the RIJ was generated as low-frequency gravity wave

Accepted for publication in *Journal of the Atmospheric Sciences*. DOI 10.1175/JAS-D-23-0047.1.

response to the thermal forcing of the convective system. Figure 10 shows the temporal evolution of the diabatic heating in the vertical plane through the bow apex (i.e., orange line in Fig. 9a). During 0230-0330 UTC, remarkable diabatic heating was found above 1.0 km MSL, peaking at about 7.0 km MSL (Figs. 10a and 10b) in the region of leading convective line. There was relatively weak diabatic heating that spread backward above 4.0 km MSL, peaking a higher altitude of about 8.0 km MSL. In contrast, the diabatic cooling was very weak (less than -0.003 K s^{-1}) which basically occurred underneath the strongest diabatic heating. The thermal forcing was confined in the leading convective line of the QLCS, with a scale of about 20~40 km. This is because the QLCS possessed a mixed feature of PS and LS precipitation rather than TS precipitation (Figs. 4 and 8). Nonetheless, as studied in Pandya and Durran (1996), it is the thermal forcing from the leading convective line that generates low-frequency gravity waves and provides the primary forcing for the generation of the RIJ. The 2D diabatic heating/cooling profile between 0230 and 0330 UTC looks most like that in Fig. 20d of Pandya and Durran (1996) which can generate an elevated RIJ. This is clearly shown in Figs. 11a and 11b that the RIJ remained to be above 2.0 km MSL, with only a few high winds (≥ 17.2 m s^{-1}) produced at the surface (Figs. 9a, 9b).

The thermal forcing was enhanced in the next hour of 0330-0430 UTC (Figs. 10c, 10d). The low-level diabatic cooling increased to more than -0.006 K s^{-1} and extended upward to more than 4.0 km MSL high. Moreover, both the diabatic heating and cooling became to tilt backward with height, similar to the thermal forcing in Fig. 20a of Pandya and Durran (1996) which can produce a descending RIJ. In response to the enhanced thermal forcing of the QLCS, which generates the low-frequency gravity waves, the RIJ intensified and descended to the surface near the gust front (Figs. 11c, 11d). The downward transport of high momentum associated with the descending RIJ (Mahoney and Lackmann 2011) produced widespread high winds of over 20 m s^{-1} at 100 m AGL (Figs. 9c, 9d).

Accepted for publication in *Journal of the Atmospheric Sciences*. DOI 10.1175/JAS-D-23-0047.1.

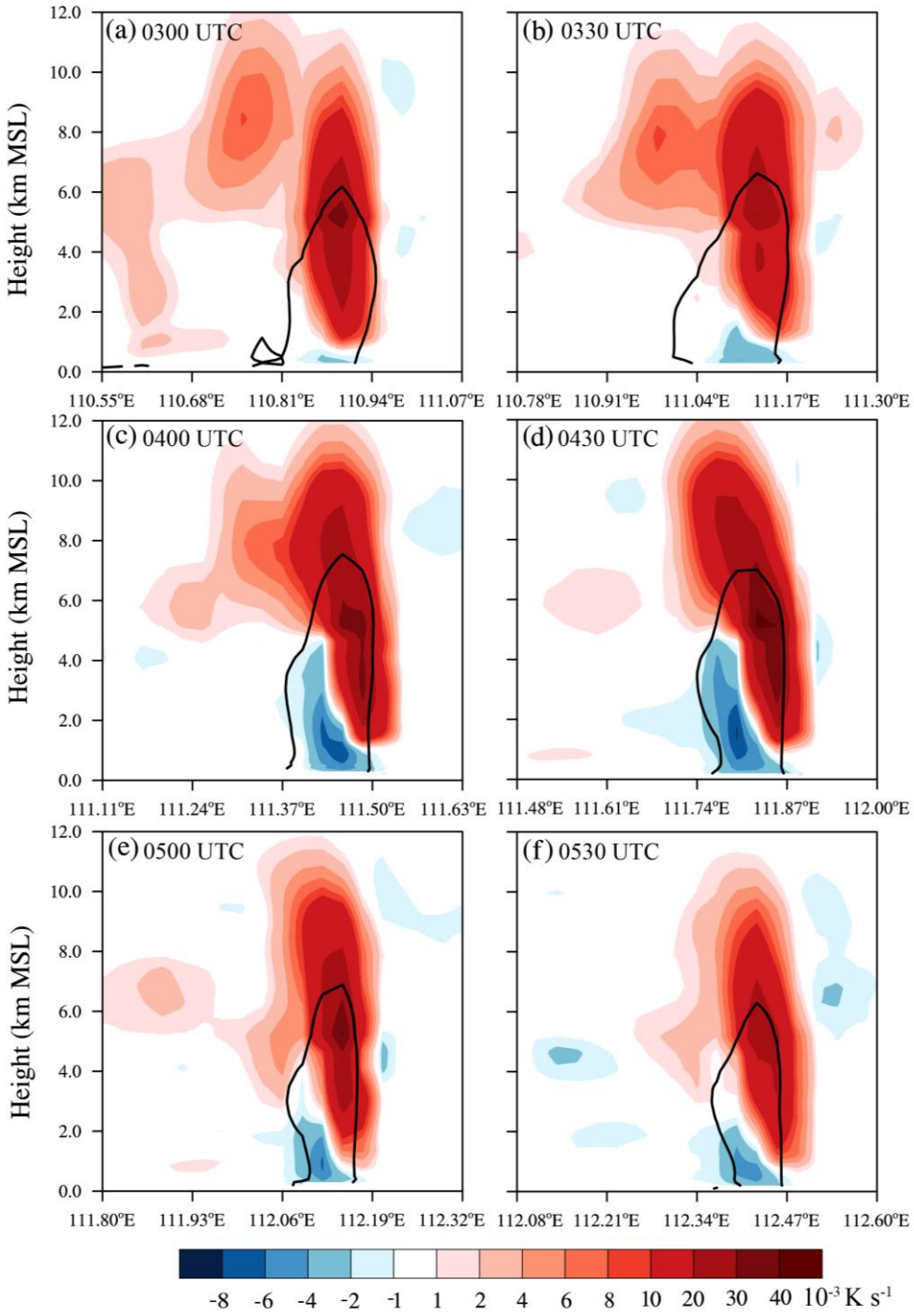

Fig. 10 Distribution of mean diabatic heating (shading; Unit: 10^{-3} K s^{-1}) in the vertical plane through the bow apex averaged during (a) 0230-0300 UTC, (b) 0300-0330 UTC, (c) 0330-0400 UTC, (d) 0400-0430 UTC, (e) 0430-0500 UTC, and (f) 0500-0530 UTC on 21 April 2017. Black line denotes the 40-dBZ reflectivity. The locations of these vertical planes are indicated by the orange lines in Figs. 9a-9f, which are averaged over the area 10 km normal to the orange lines.

Accepted for publication in *Journal of the Atmospheric Sciences*. DOI 10.1175/JAS-D-23-0047.1.

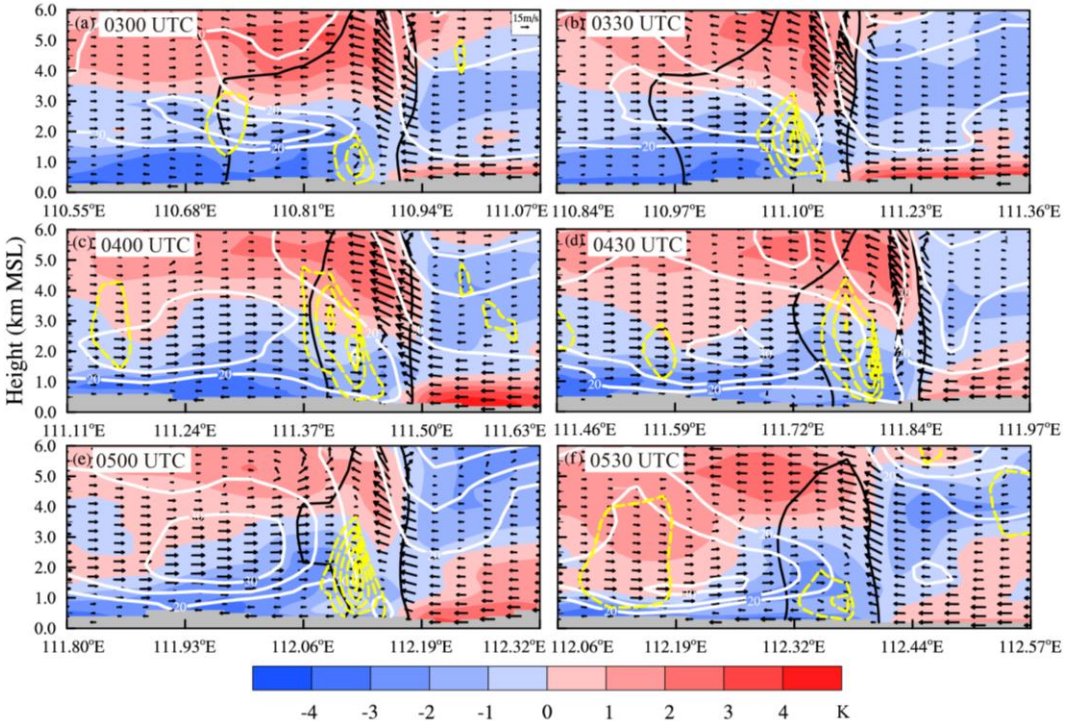

Fig.11 Simulated system-relative winds (vectors; the vertical velocity is exaggerated by 5 times for clear visualization), ground-relative horizontal wind speed (white contours; unit: m s^{-1}), and perturbed temperature (shading; unit: K) in the vertical plane near the bow apex at (a) 0300 UTC, (b) 0330 UTC, (c) 0400 UTC, (d) 0430 UTC, (e) 0500 UTC, and (f) 0530 UTC on 21 April 2017. Black line denotes the 40-dBZ reflectivity, whereas yellow dashed contours are for the downdrafts plotted at every -0.5 m s^{-1}. The locations of these vertical planes are indicated by the orange lines in Figs. 9a-9f, which are averaged over the area 10 km normal to the orange lines.

The elevated RIJ descent was also amplified by downdrafts developing at its leading edge. At 0300 UTC (Fig. 11a), the downdrafts only occurred at low levels below 2.0 km MSL, which intensified to more than -2 m s^{-1} and extended upwards to 3.0 km MSL at 0330 UTC (Fig. 11b). According to Adams-Selin and Johnson (2013), the enhancement of low-level diabatic cooling can strengthen the downdrafts by wind flows generated by low-frequency gravity waves. To better understand the development of downdrafts, the vertical momentum equation was analyzed as in Xu et al. (2015b) , i.e.,

$$\frac{Dw}{Dt} = -\frac{1}{\bar{\rho}}\frac{\partial p'_d}{\partial z} - \frac{1}{\bar{\rho}}\frac{\partial p'_b}{\partial z} + \boldsymbol{b}, \quad (1)$$

Accepted for publication in *Journal of the Atmospheric Sciences*. DOI 10.1175/JAS-D-23-0047.1.

where $\boldsymbol{p'_d}$ is the dynamic pressure perturbation given by

$$\nabla^2 p'_d = -\nabla \cdot (\bar{\rho}\mathbf{V} \cdot \nabla \mathbf{V}), \tag{2}$$

with **V** = (*u*, *v*, *w*) being the three-dimensional velocity vector, *b* is the buoyancy, i.e.,

$$\boldsymbol{b = g\left[\frac{\theta-\bar{\theta}}{\bar{\theta}} + 0.61(q_v - \overline{q_v}) - q_h\right]}, \tag{3}$$

and $\boldsymbol{p'_b}$ is the buoyancy-induced pressure perturbation given by

$$\nabla^2 p'_b = \frac{\partial \bar{\rho} b}{\partial z}. \tag{4}$$

In these equations, g is the gravitational acceleration, ρ is the air density, θ is the potential temperature, and q_h is the sum of both liquid and solid hydrometeor mixing ratio, with the steady base-state variables denoted by overbar. (The base state is defined as the areal mean within a 1°×1° box in the inflow region averaged between 0300 and 0700 UTC, with an example of the box given in Fig. 8b).

The first two terms on the right-hand side (RHS) of Eq. (1) designate the vertical pressure gradient forces (PGFs) owing to dynamical and buoyancy-induced pressure perturbations, respectively (i.e., PGF_D and PGF_B). The last one is the buoyancy term which, according to Eq. (3), can be divided into contributions from the potential temperature and water vapor perturbations (i.e., virtual temperature; B_TV) and hydrometeor loading (B_HL). These four terms in the vertical plane along the RIJ and their sum (i.e., total vertical acceleration) are given in Fig. 12.

Accepted for publication in *Journal of the Atmospheric Sciences*. DOI 10.1175/JAS-D-23-0047.1.

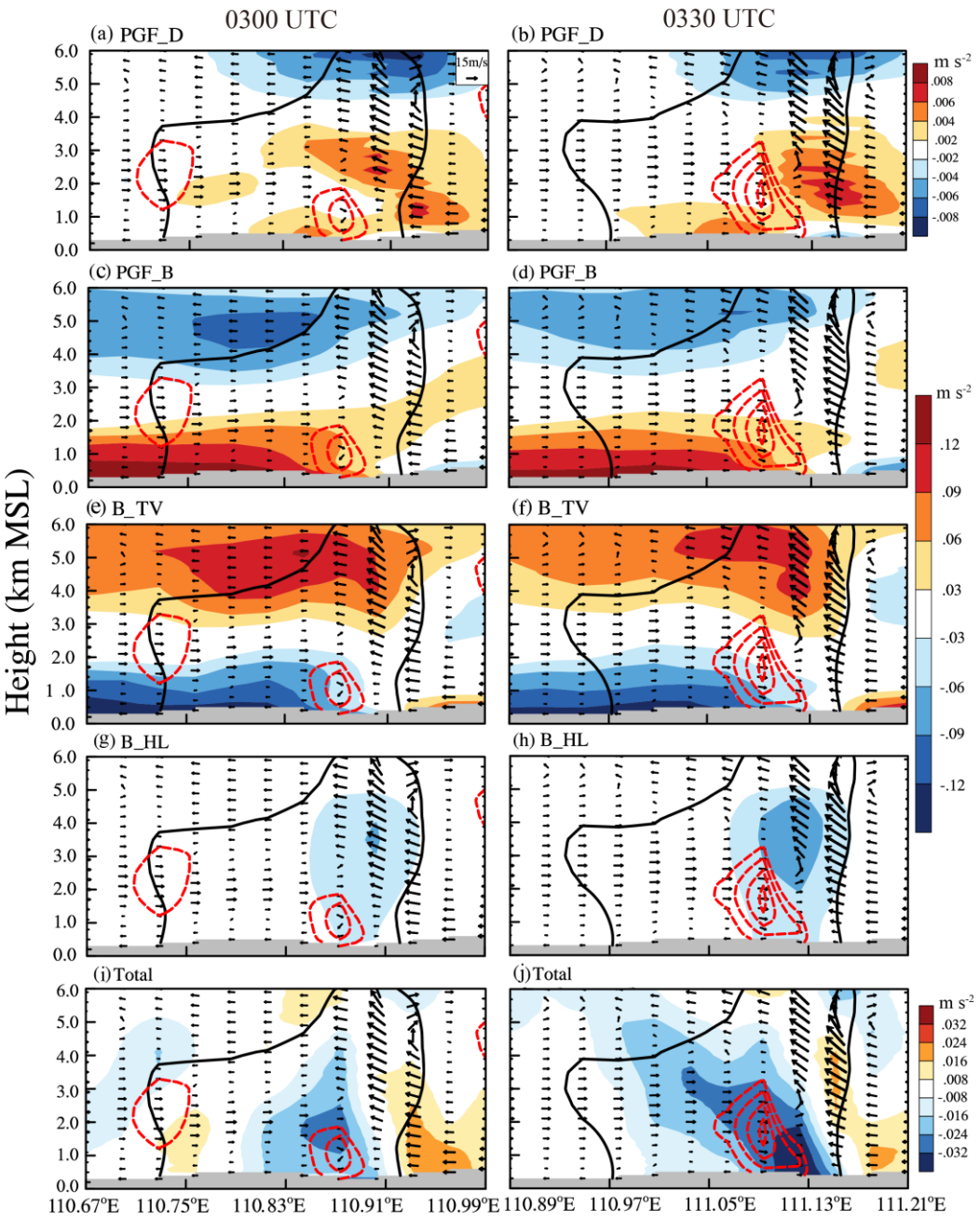

Fig.12 Simulated vertical pressure gradient forces (shading; unit: m s^{-2}) caused by (a) dynamical pressure perturbation (PGF_D) and (c) buoyancy-induced pressure perturbation (PGF_B), buoyancy due to virtual temperature perturbation (B_TV) and (g) hydrometeor loading (B_HL), and (i) total vertical acceleration in the vertical plane near the bow apex at 0300 UTC on 21 April 2017. Also shown are the system-relative winds (vectors; the vertical velocity is exaggerated by 5 times for clear visualization), 40-dBZ radar reflectivity (black solid contour) and downdrafts (red dashed contours at an interval of -0.5 m s^{-1}). The right panel is the same as left except at 0330 UTC. The locations of the vertical planes are indicated by the orange lines in Figs. 9a and 9b.

Accepted for publication in *Journal of the Atmospheric Sciences*. DOI 10.1175/JAS-D-23-0047.1.

At 0300 UTC, both the PGF_D and PGF_B terms were positive in the downdraft region at the RIJ leading edge, with the former one order smaller than the latter (Figs. 12a, 12c). The low-level positive PGF_B resulted from the buoyancy-induced pressure deficit centered around 3.0 km MSL (not shown). By contrast, the other two terms of B_TV and B_HL were negative, especially the former (Figs. 12e, 12g). Therefore, the occurrence of downdrafts at this early time was mainly attributed to the negative buoyancy of the cold pool. At 0330 UTC, the PGF_D and PGF_B terms were still positive in the downdraft region (Figs. 12b, 12d). The PGF_B term weakened below about 1.5 km MSL, thus favoring the development of downdraft in the boundary layer. The negative B_TV term changed little (Fig. 12f), because the low-level latent cooling and hence cold pool intensity hardly changed over time (Figs. 11a, 11b). Yet, the B_HL term was enhanced between about 2.0-4.5 km MSL (Fig. 12h), indicating that the hydrometeor loading played a vital role in the strengthening and upward extension of the downdrafts at the cold pool leading edge.

From 0430 UTC, the diabatic heating gradually weakened and lacked its feature of backward tilt (Figs. 10e and 10f), given the decaying of convection in the central and southern parts of the bow echo (Figs. 8e-g). Consequently, the downdrafts weakened and the RIJ became elevated again above 1.5 km MSL (Figs. 11e, 11f) which reduced the downward transport of high momentum. The near-surface high winds thus ceased at the bow apex (Fig. 9f).

4.3 High winds in the merger stage

Both the intensity and area of high winds were significantly enhanced in the merger stage (Figs. 6, 7, and 9). It agrees with the finding of French and Parker (2012) that the merger can help strengthen the damaging surface winds. In the study of idealized squall line-supercell merger (French and Parker 2014), the more severe winds were attributed to the locally enhanced cold pool in the merger area which in turn strengthened the RIJ. In this case, however, the cold pool was not enhanced by the merger.

Accepted for publication in *Journal of the Atmospheric Sciences*. DOI 10.1175/JAS-D-23-0047.1.

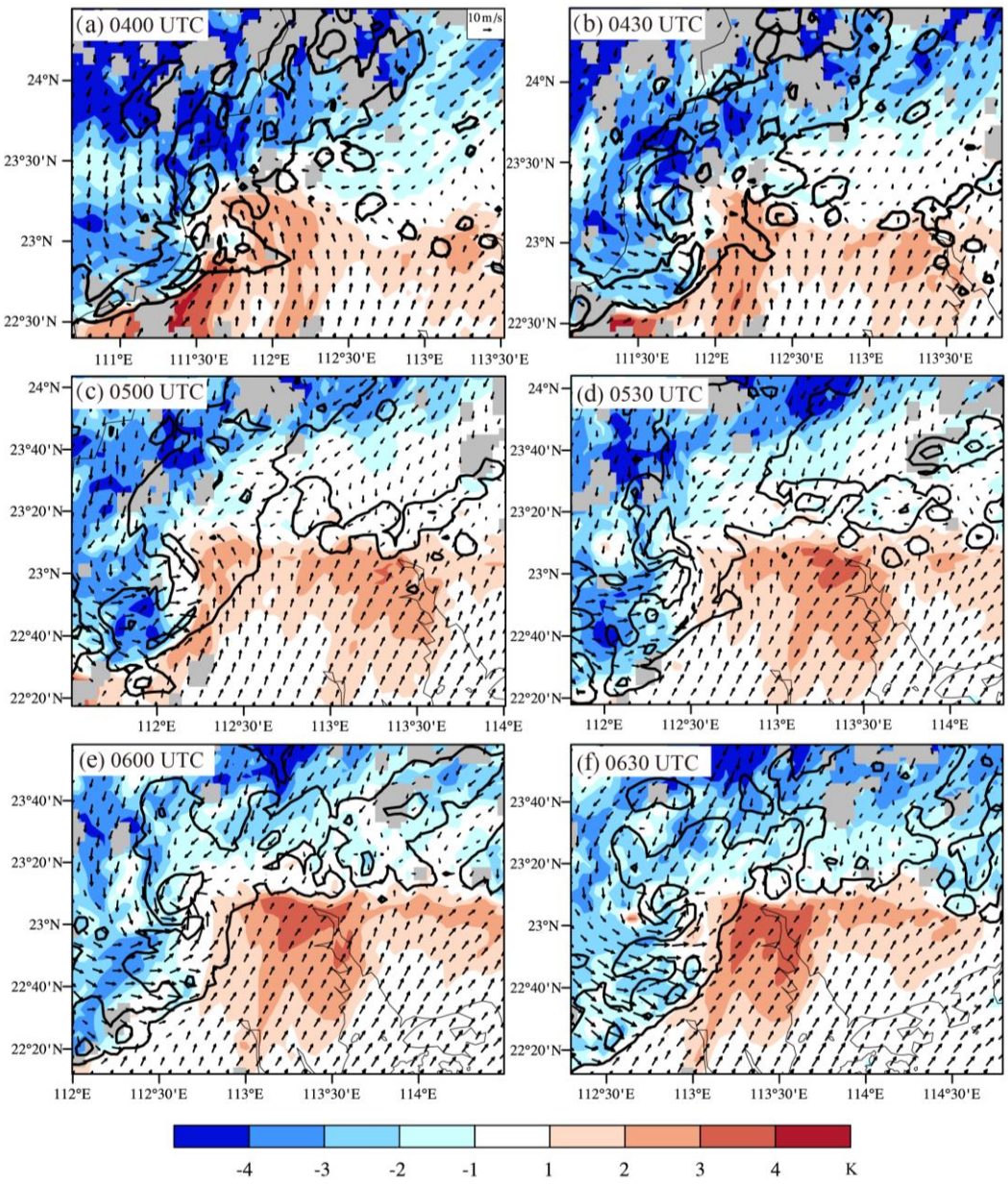

Fig. 13 Simulated temperature perturbations (shading; unit: K) and horizontal winds (vectors) at 500 m MSL at (a) 0400 UTC, (b) 0430 UTC, (c) 0500 UTC, (d) 0530 UTC, (e) 0600 UTC, and (f) 0630 UTC on 21 April 2017. Black contours are the composite reflectivity of 35 and 50 dBZ.

Figure 13 shows the temperature perturbations at 500 m MSL. (This height is close to the surface given the terrain in Guangdong province.) At 0400 UTC (Fig. 13a), the cold pool of the bow echo was generally 2-4 K colder due to the weak diabatic cooling. To the east of the bow echo, there was a convergence line at about 23°20'N, with cold northerlies from the north and warm southerlies from the south, respectively. This line is actually part of the synoptic-scale shear line (Fig. 2d). Benefiting from the large-scale convergence, scattered convective cells developed along the shear line which organized

Accepted for publication in *Journal of the Atmospheric Sciences*. DOI 10.1175/JAS-D-23-0047.1.

into a zonal convective line at 0500 UTC (Figs. 13b and 13c). In the next two hours, the convective line gradually merged with the northern part of the bow echo (Figs. 13d-13f). During the merger, there was little increase in the intensity of the cold pool which remained to be 2-4 K colder. Indeed, the cold pool in the central and southern parts of the bow echo showed a weakening trend with time, due to the dissipation of convections there. However, the RIJ did not get weakened, and was even stronger than in the early stage, as revealed by the isoline of 35 m s^{-1} at 1.5 km MSL (Fig. 9g). The jet core was evidently biased to the north of the bow apex where a cyclonic vortex was present (Figs. 9f-9i). With a diameter of ~40-60 km, this meso-β-scale vortex appeared to be the cyclonic one of the line-end vortex pair that formed at the two ends of QLCSs, which can enhance the RIJ (e.g., Weisman and Davis 1998; Meng et al. 2012).

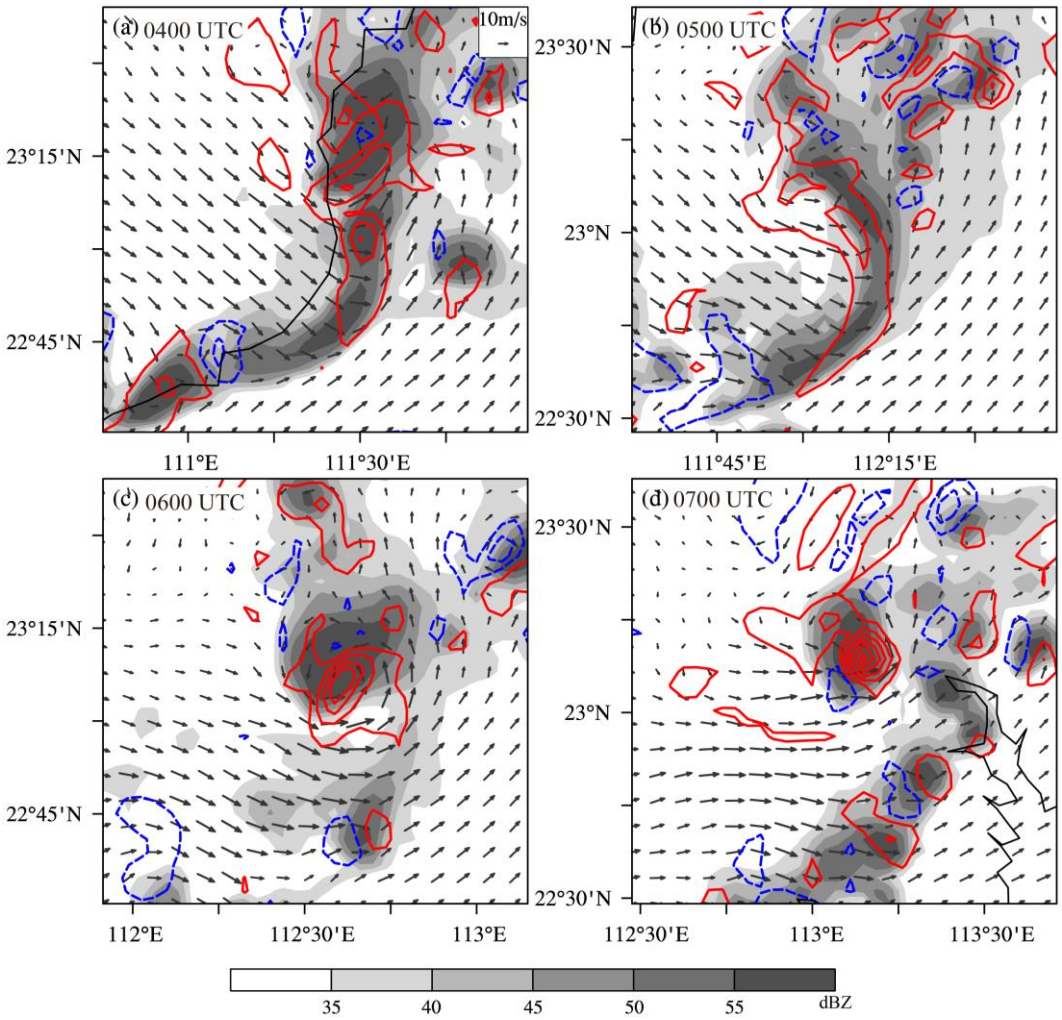

Fig. 14 Simulated horizontal winds (vectors) and vertical vorticity (contours; unit: s^{-1}) at 1500 m MSL at (a) 0400 UTC, (b) 0500 UTC, (c) 0600 UTC, and (d) 0700 UTC on 21 April 2017. Positive

Accepted for publication in *Journal of the Atmospheric Sciences*. DOI 10.1175/JAS-D-23-0047.1.

and negative vertical vorticity are denoted by red and blue lines, respectively, which start from $\pm 1\times10^{-3}$ s^{-1} at an interval of $\pm 2\times10^{-3}$ s^{-1}. Grey shadings are the composite reflectivity (unit: dBZ).

Figure 14 depicts the evolution of the relative vertical vorticity (hereafter, vertical vorticity for simplicity) at 1.5 km MSL. The leading convective line of the QLCS was dominated by positive vertical vorticity, especially in its northern part. Negative vertical vorticity was found at the southern end which was relatively weak. This asymmetric development of the line-end vortex pair is likely due to the Coriolis forcing that inhibits the anti-cyclonic circulation via vertical stretching of planetary vorticity as the system lifetime extends past 1/*f* for approximately 3 hours (Skamarock et al. 1994). During the merger, the cyclonic circulation became more concentrated in the northern part of the convective system, with the maximum vertical vorticity increased from 5.4×10^{-3} s^{-1} at 0400 UTC to 1.1×10^{-2} s^{-1} at 0700 UTC (Figs. 13a, 13d). In response to the vortex intensification, stronger northwesterly/westerly winds were induced along the southern flank of the vortex than in the early stage, which helped enhance/maintain the RIJ in the merger stage.

Although the RIJ was strong in the merger stage, the near-surface high winds were not produced by the descent of the RIJ. This is clearly shown in Fig. 15 which presents the horizontal wind speed and vertical velocity in the vertical plane across the maximum near-surface high wind at 0600 UTC (see its location in Fig. 9g). The RIJ was elevated above 2 km MSL, below which there were updrafts (over 3 m s^{-1}) rather than downdrafts.

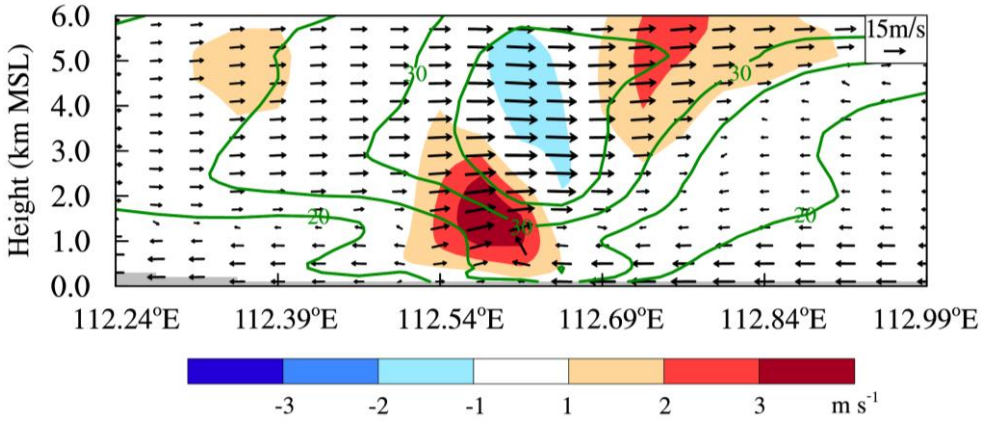

Fig.15 Simulated system-relative winds (vectors; the vertical velocity is exaggerated by 5 times for clear visualization), ground-relative horizontal wind speed (dark green contours; unit: m s^{-1}), and

Accepted for publication in *Journal of the Atmospheric Sciences*. DOI 10.1175/JAS-D-23-0047.1.

vertical velocity (shading; unit: m s^{-1}) in the vertical plane across the high-wind center at 100 m ALG at 0600 UTC on 21 April 2017. The location of the vertical plane is given by the orange line in Fig. 9g.

To better reveal the origin of near-surface high winds, the trajectories of air parcels within the region of horizontal wind speed of > 20 m s^{-1} at 100 m AGL (Fig. 9g) were examined. A number of 30 parcels were released at 0600 UTC and traced backward for 60 minutes. The parcel trajectories were calculated using the WRF model output at 3-min interval based on a fourth-order Runge-Kutta scheme (e.g., Xu et al. 2017; Wei et al. 2022). As shown in Fig. 16a, these parcels came from both northeast and southeast of the bow echo, depending on their final locations. More importantly, these parcels came from the low level below 500 m AGL (Fig. 16c). For comparison, the backward trajectories of air parcels within the high-wind region near the bow apex at 0500 UTC (i.e., early stage) were also calculated. Different from in the merger stage, most of these parcels came from above 3 km AGL behind the bow echo (Figs. 16b, 16d), which were in association with the descending RIJ.

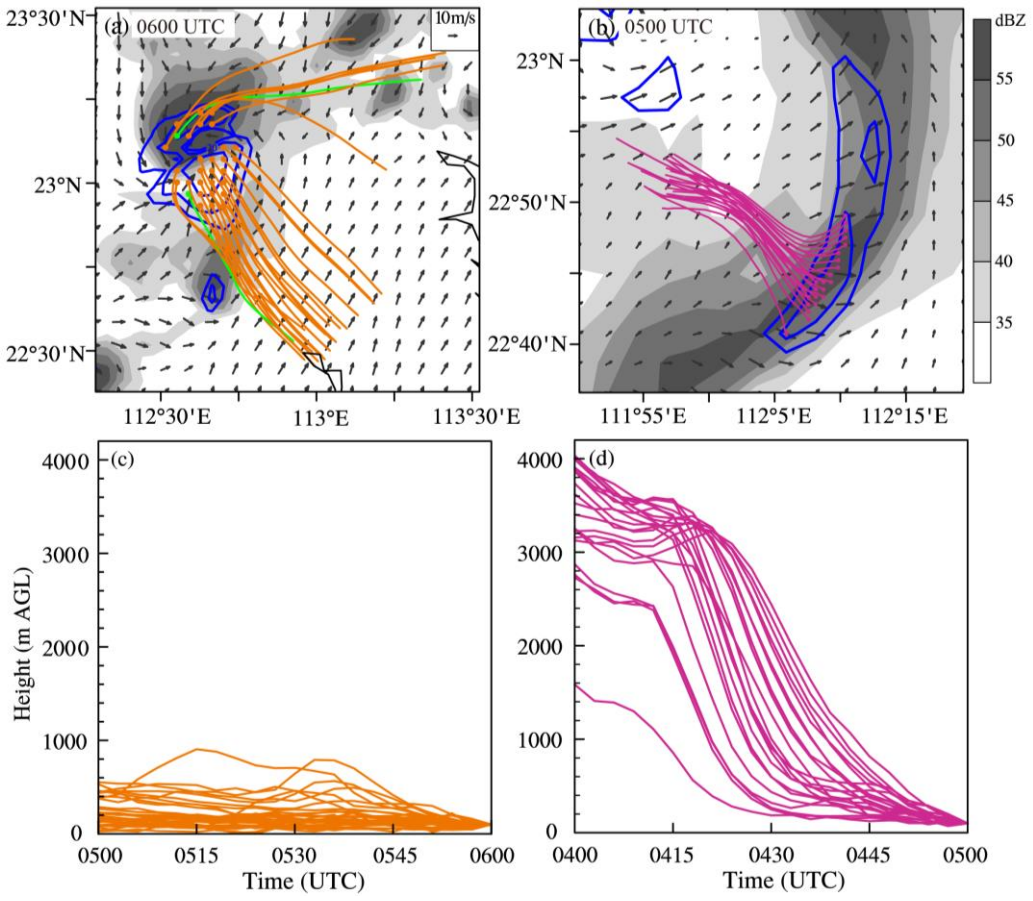

Accepted for publication in *Journal of the Atmospheric Sciences*. DOI 10.1175/JAS-D-23-0047.1.

Fig. 16 (a) The 1-hour (0500-0600 UTC) backward trajectories of air parcels in the region of high winds > 20 m s^{-1} at 100 m AGL. Also shown are the horizontal winds (vectors) and speed (17.2 m s^{-1}, 20 m s^{-1}, 25 m s^{-1} and 30 m s^{-1}; blue contours) at 100 m AGL and composite reflectivity (shading; unit: dBZ) at 0600 UTC on 21 April 2017. The two parcels analyzed in Fig. 19 are colored in green. (b) Same as (a) but for the 1-hour (0400-0500 UTC) backward trajectories of air parcels near the bow apex. (c) and (d) are the time evolution of parcel heights.

For the generation of high winds in the merger stage, the fact that the RIJ remained elevated and the high-wind air parcels originated from low altitudes implied a different mechanism from the descent of RIJ in the early stage. Note that the high winds occurred on the southern flank of the cyclonic line-end vortex (Fig. 9g). It suggested that the low-level rotation of the vortex played an important role in enhancing the near-surface high winds, similar to the enhancement of RIJ by the mid-level rotation. At 0500 UTC (Fig. 17a), the peak vertical vorticity at 500 m MSL was 4.8×10^{-3} s^{-1}, located behind (i.e., to the west of) the leading convective line. Over time, the vertical vorticity wrapped cyclonically into the region of deep convection featured by high reflectivity (Figs. 17b-17d). The low-level rotation achieved its peak intensity at 0700 UTC when the maximum vertical vorticity reached 9.7×10^{-3} s^{-1} (Fig. 17e). Then the low-level rotation decreased rapidly at 0730 UTC (Fig. 17f).

Accepted for publication in *Journal of the Atmospheric Sciences*. DOI 10.1175/JAS-D-23-0047.1.

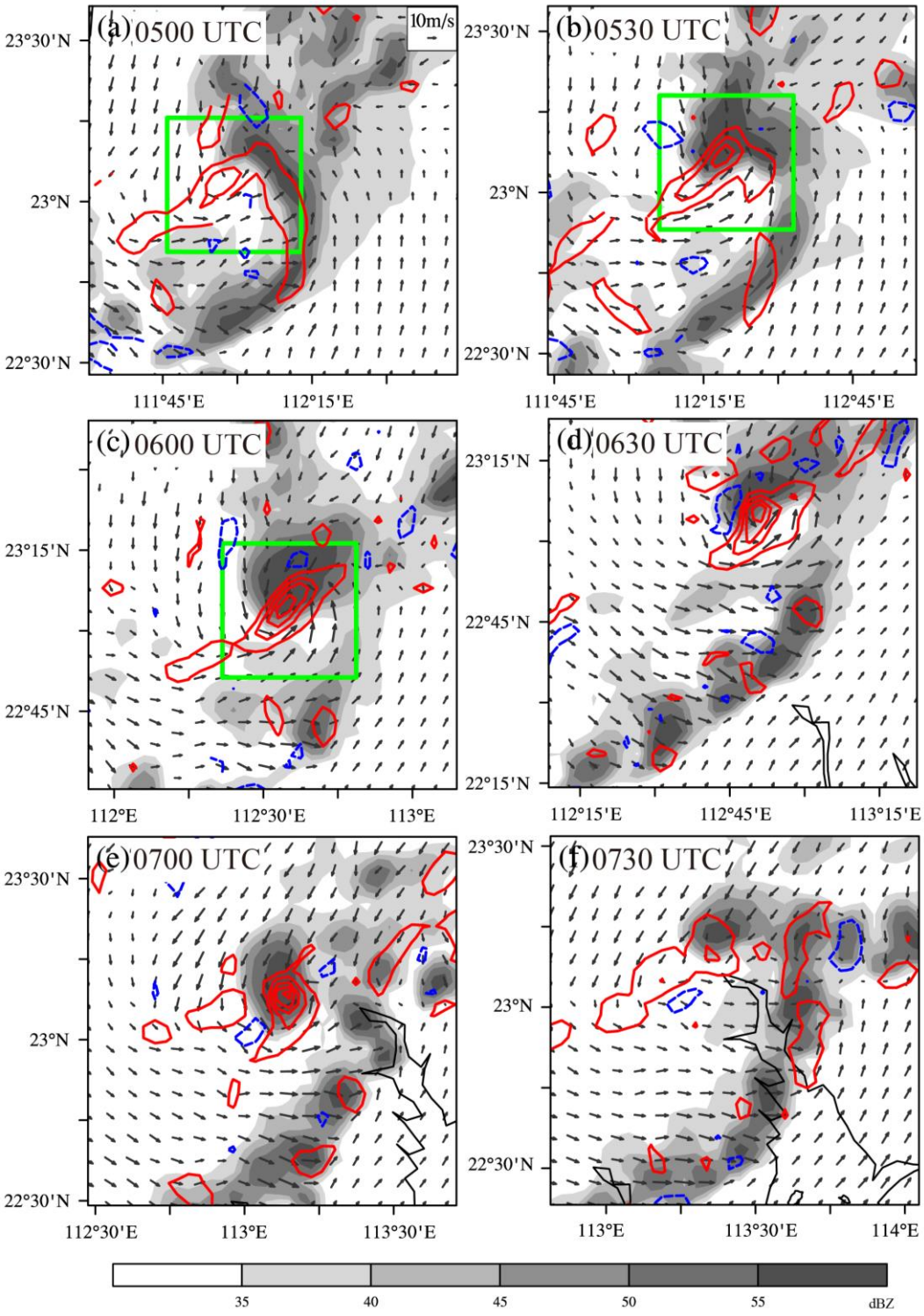

Fig. 17 Simulated horizontal winds (vectors) and vertical vorticity (contours; unit: s^{-1}) at 500 m MSL at (a) 0500 UTC, (b) 0530 UTC, (c) 0600 UTC, (d) 0630UTC, (e) 0700 UTC and (f) 0730 UTC on 21 April 2017. Positive and negative vertical vorticity are denoted by red and blue lines, respectively, which start from $\pm 1\times10^{-3}$ s^{-1} at an interval of $\pm 2\times10^{-3}$ s^{-1}. The composite reflectivity is shaded (unit: dBZ). Green boxes in (a)-(c) denote the region for the calculation of mean vertical

Accepted for publication in *Journal of the Atmospheric Sciences*. DOI 10.1175/JAS-D-23-0047.1.

vorticity in Fig. 18.

The rapid increase of the vertical vorticity at 500-m MSL indicated a downward development of the line-end vortex in the merger stage. At 0500 UTC, the maximum vertical vorticity was located at ~2.0 km MSL, which gradually lowered to about 0.5 km MSL at 0700 UTC (Fig. 18). The changes of vertical vorticity can be explained according to its budget equation

$$\frac{\partial \zeta}{\partial t} = -(\mathbf{V}_h - c)\cdot\nabla\zeta - w\frac{\partial \zeta}{\partial z} - (f+\zeta)\left(\frac{\partial u}{\partial x}+\frac{\partial v}{\partial y}\right) - \left(\frac{\partial w}{\partial x}\frac{\partial v}{\partial z} - \frac{\partial w}{\partial y}\frac{\partial u}{\partial z}\right), \quad (5)$$

where ζ is the relative vertical vorticity, $\boldsymbol{V_h} - c$ is the system-relative wind, f is the Coriolis parameter (also known as planetary vorticity), and $\mathbf{V}_h = (u, v)$ and w are the horizontal and vertical velocities, respectively. The first and second terms on the RHS of Eq. (5) are the horizontal and vertical advections (HAD and VAD) of relative vertical vorticity, respectively. The third term indicates the vertical stretching (STR) of absolute vertical vorticity (i.e., relative vertical vorticity plus planetary vorticity), with the last one denoting the vertical tilting term (TLT).

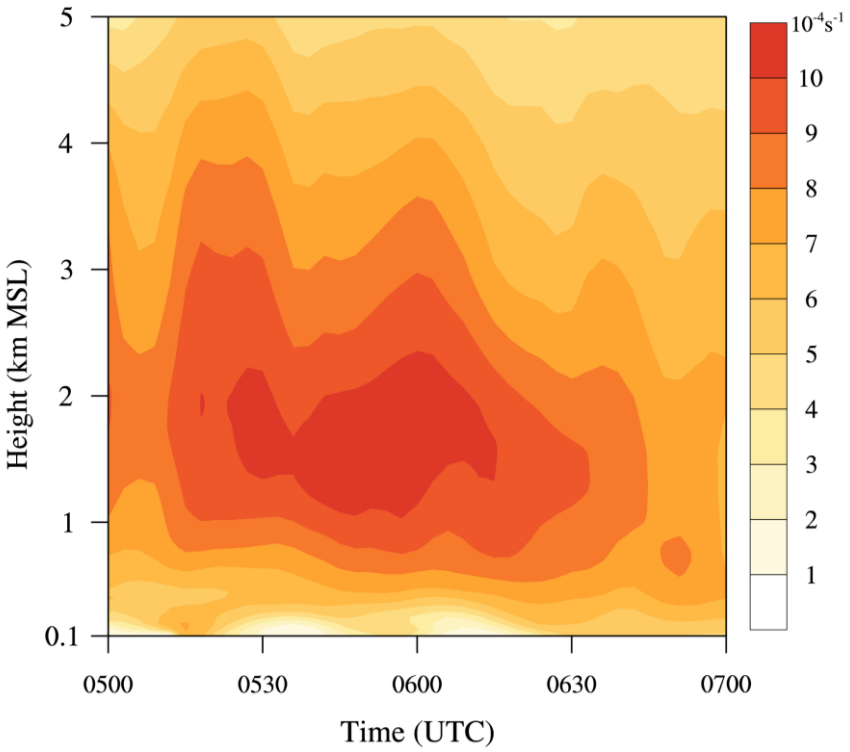

Fig. 18 Time-height plot of the vertical vorticity (shading; unit: 10^{-4} s^{-1}) averaged within the box encompassing the vortex at the northern end of the bow echo.

Figure 19a presents the evolution of the vertical vorticity at 500 m MSL between

Accepted for publication in *Journal of the Atmospheric Sciences*. DOI 10.1175/JAS-D-23-0047.1.

0500 and 0600 UTC averaged within a 48 km × 48 km box encompassing the vortex (see Figs. 17a-17c), along with individual budget terms given in Fig. 19b. The vertical vorticity integrated according to Eq. (5) was in good agreement with that interpolated from the model output. The box-mean vertical vorticity increased by about 40% during this time. The HAD term contributed negatively, because of the relatively weak vertical vorticity outside the vortex. The VAD term also had a negative contribution, given the low-level updrafts (Fig. 15) and positive $\frac{\partial \zeta}{\partial z}$ in the vortex region. The latter was owing to that the vertical vorticity generally increased with height below about 2 km MSL (Fig. 18). The increase of the low-level vertical vorticity was thus caused by the TLT and STR terms, especially the latter which had a contribution about three times of that of the TLT.

The importance of STR in enhancing the vertical vorticity can also be revealed by the budget of vertical vorticity following air parcel's trajectory, i.e.,

$$\frac{D\zeta}{Dt} = -(f+\zeta)\left(\frac{\partial u}{\partial x}+\frac{\partial v}{\partial y}\right) - \left(\frac{\partial w}{\partial x}\frac{\partial v}{\partial z} - \frac{\partial w}{\partial y}\frac{\partial u}{\partial z}\right). \quad (6)$$

Lagrangian vertical vorticity budgets are conducted for the high-wind parcels in Fig. 16a during the period of 0530-0600 UTC. Before 0530 UTC, these parcels were far away from the bow echo, especially for those coming from the southeast direction. Two parcels (i.e., P1 and P2 denoted by the green trajectories in Fig. 16a) are selected which represent the parcels coming from the southeast and northeast directions, respectively. P1 and P2 were close to the maxima of vertical vorticity which was located between the two maxima of the horizontal wind speed (see Fig. 22a). As shown in Figs. 19c and 19d, the initial vertical vorticity of the two parcels was very weak at 0530 UTC which increased rapidly in the next 30 minutes. For P1 from the southeast, the increase of vertical vorticity was dominated by the STR term (Fig. 19c). Yet, it was the TLT term that was responsible for the vertical vorticity growth of P2 from northeast. The different mechanisms of vertical vorticity intensification are due to that the parcels coming from southeast finally reached the region of evident convergence at 0600 UTC while their northeast analogue terminated in the region of weak convergence and even divergence (Fig. 20a). Nevertheless, for the average of high-wind parcels, the increase of vertical

Accepted for publication in *Journal of the Atmospheric Sciences*. DOI 10.1175/JAS-D-23-0047.1.

vorticity was primarily induced by the STR term, consistent with the case of box mean (i.e., Eulerian framework). This is because most of the high-wind parcels came from southeast which experienced significant low-level convergence (Fig. 20a).

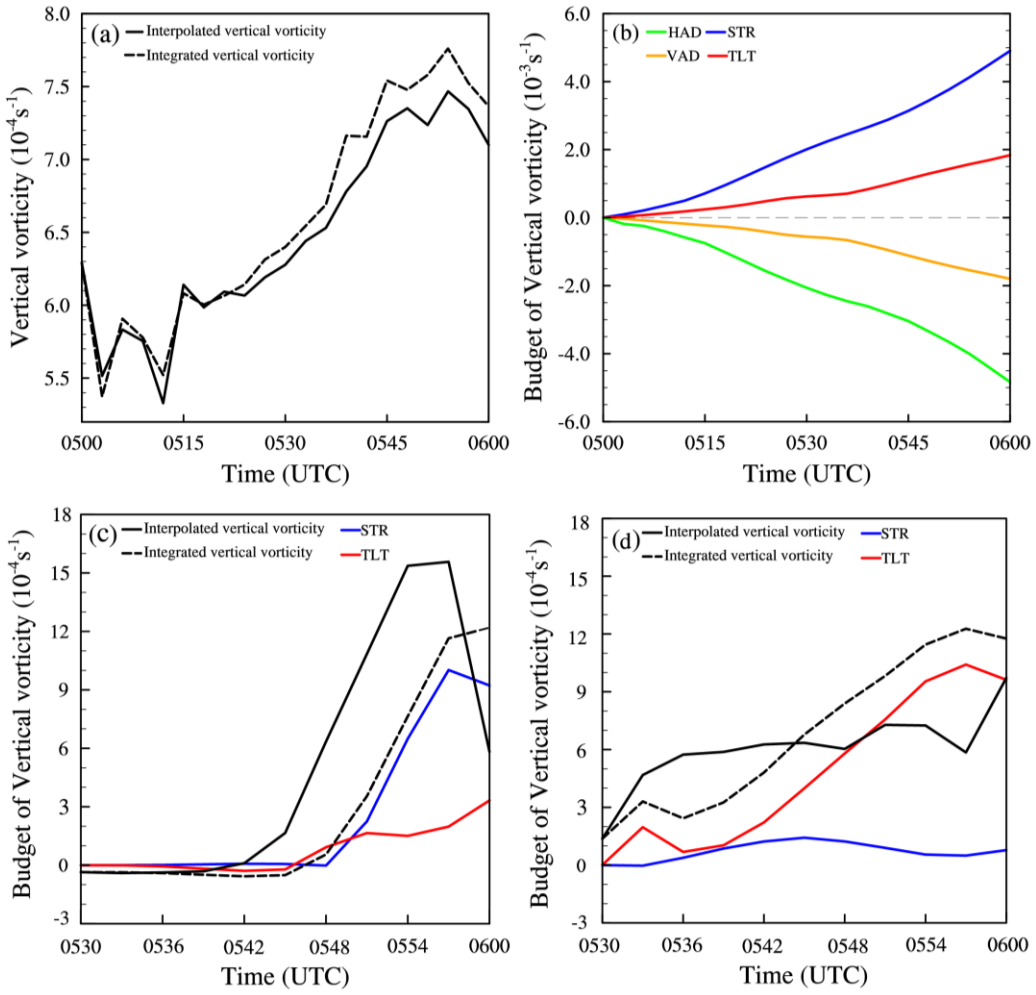

Fig. 19 (a) Time evolution of mean vertical vorticity averaged in the region of the low-level vortex (see the green boxes in Figs. 17a-17c) at 500 m MSL between 0500 and 0600 UTC on 21 April 2017, with the horizontal and vertical advection terms (HAD and VAD), and titling (TLT) and stretching (STR) terms shown in (b). (c) and (d) are, respectively, the Lagrangian vertical vorticity budgets for two representative air parcels (P1 and P2, see Fig. 16a) terminating in the high-wind region of 100 m MSL at 0600 UTC. Solid and dashed black lines in (a), (c) and (d) represent the vertical vorticity interpolated from the model output and integrated according to the budget equations of vertical vorticity, respectively.

The major role of the STR term in enhancing the vertical vorticity indicates the importance of convergence in the development of low-level vortex. As shown in Fig.

Accepted for publication in *Journal of the Atmospheric Sciences*. DOI 10.1175/JAS-D-23-0047.1.

20a, local convergence stronger than -7×10^{-3} s^{-1} was found near the intense convection of composite reflective >50dBZ in the northern bow echo. Weaker but more widespread convergence was found to the east where the large-scale shear line was present (Fig. 13). Figure 20b gives the evolution of the mean convergence averaged in the northern part of the bow echo where it interacted with the large-scale shear line and merged with the convection to its east. During 0330 and 0430 UTC, the low-level convergence firstly increased and then decreased, consistent with the evolution of the bow echo. That is, the leading convective line (of composite reflectivity > 45dBZ) was continuous at 0330 and 0400 UTC which, however, was segmented at 0430 UTC (Figs. 8a, b, d). The low-level convergence turned to increase again from 0430 UTC, which also agreed with the redevelopment of the bow echo as evidenced by its continuous convective line at 0500 UTC (Fig. 8e). At 0430 UTC, scattered convective cells were just developed along the large-scale shear line which had not yet merged with the bow echo (Figs. 8d and 13b). Note that the northern part of the bow echo intersected the large-scale shear line, to the north of which the prevailing northerlies intensified with time since 0400 UTC (Fig. 21). In response to the enhanced large-scale convergence, the decaying QLCS became redeveloped, similar to the initiation and organization of convective cells along the shear line. As these cells evolved into a zonal convective line and merged with the bow echo after 0500 UTC, the peak intensity of convection (in terms of maximum composite reflectivity) in the northern bow echo intensified (Figs. 8 and 13), with the low-level convergence enhanced more notably (Fig. 20b). This led to the rapid intensification of low-level vortex through vertical stretching of vertical vorticity (Fig. 19).

Accepted for publication in *Journal of the Atmospheric Sciences*. DOI 10.1175/JAS-D-23-0047.1.

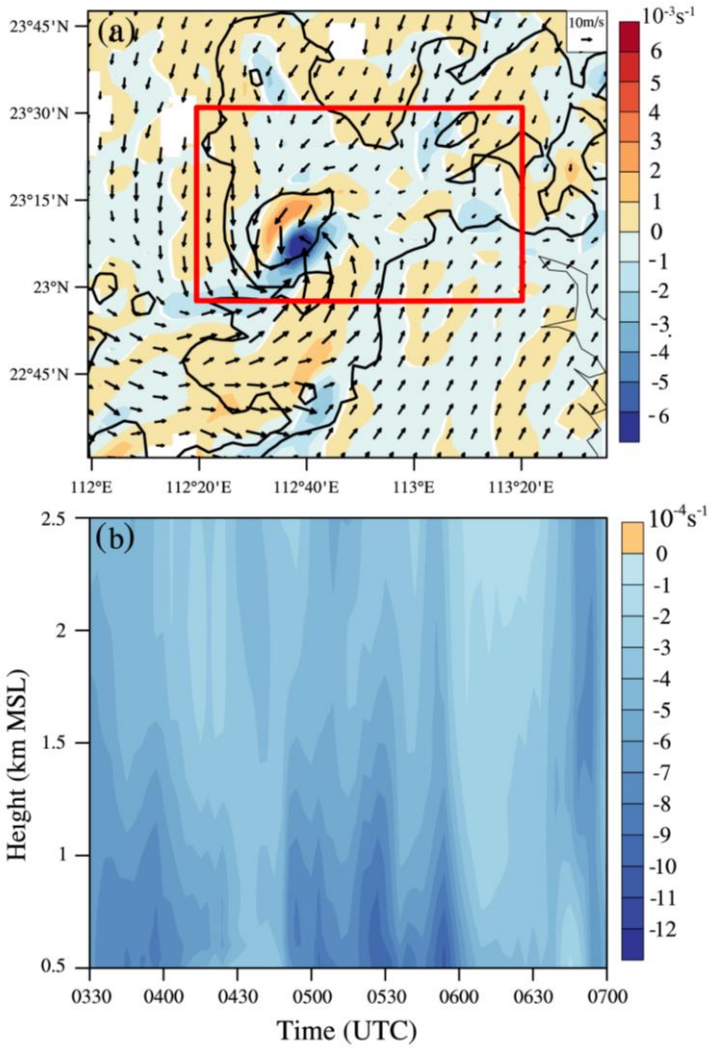

Fig. 20 (a) Simulated horizontal winds (vectors) and convergence (shading; unit: 10^{-3} s^{-1}) at 500 m MSL at 0600 UTC on 21 April 2017. Black contours are the composite reflectivity of 35 and 50 dBZ. (b) Time-height plot of horizontal convergence (shading, unit: 10^{-4} s^{-1}) averaged within the box in (a) that covers the northern bow echo where the system interacted with the large-scale shear line and merged with the convection to its east.

Accepted for publication in *Journal of the Atmospheric Sciences*. DOI 10.1175/JAS-D-23-0047.1.

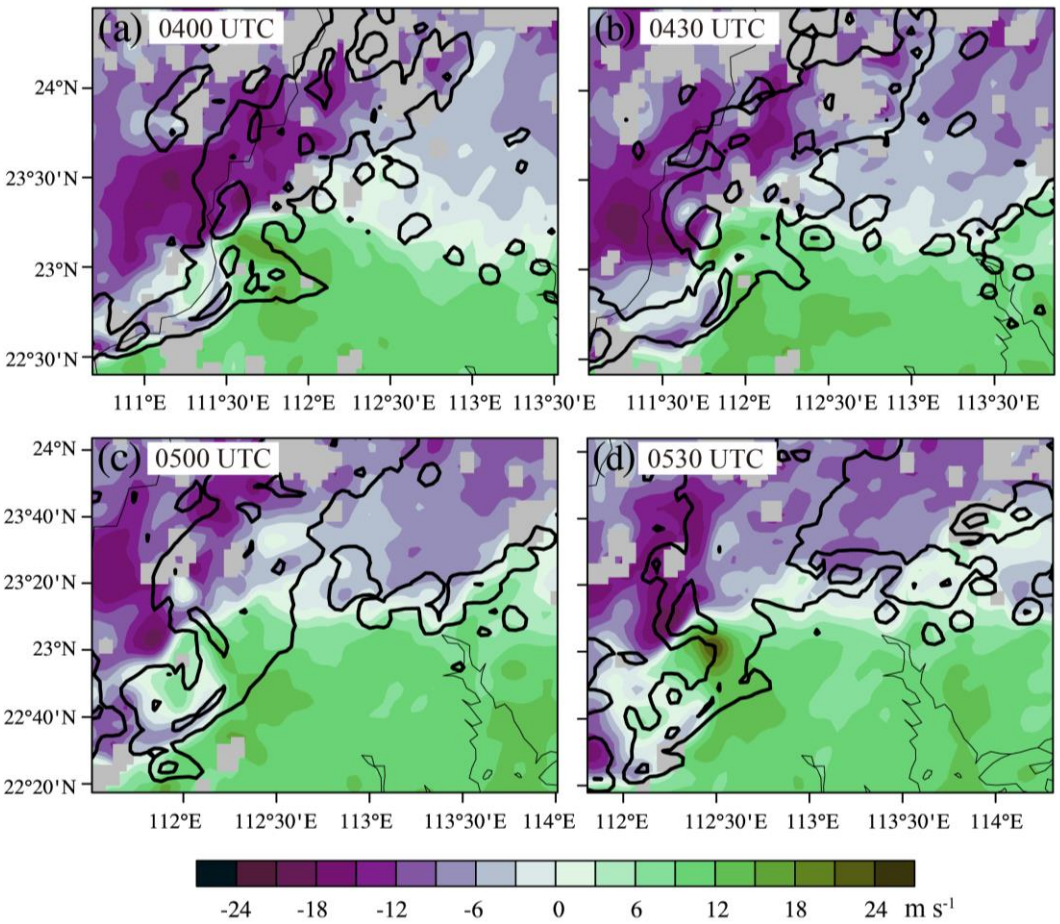

Fig. 21 Simulated meridional wind (shading; unit: m s^{-1}) at 500 m MSL at (a) 0400 UTC, (b) 0430 UTC, (c) 0500 UTC, and (d) 0530 UTC on 21 April 2017. Black contours are the composite reflectivity of 35 and 50 dBZ.

Finally, to quantify the contribution of low-level vortex to the near-surface high winds, the rotational horizontal winds were retrieved from the vertical vorticity field at 100 m AGL by solving a two-dimensional Poisson equation of streamfunction as in Wakimoto et al. (2006) and Xu et al. (2015b). Then the rotational parts were subtracted from the total horizontal winds to obtain the horizontal winds without low-level vortex. Figures 22a and 22b compare the horizontal winds at 100-m AGL with and without the vortex at 0600 UTC for an example. In the presence of the low-level vortex, high winds of over 20 m s^{-1} mainly occurred on the southeastern flank of the vortex. When the vortical flow is removed, the area of high winds shrinks considerably, with the high-wind center shifted northward by about 20 km. Thus, the vortex acts to enhance the horizontal wind speed on its southern side where the vortical flow is in the same

Accepted for publication in *Journal of the Atmospheric Sciences*. DOI 10.1175/JAS-D-23-0047.1.

direction as the ambient flow (e.g., Wakimoto et al. 2006; Atkins and Laurent 2009; Xu et al. 2015b). By contrast, the maximum wind speed north of the vortex is weakened by ~5 m s^{-1}. It suggests that the low-level vortex is able to increase the area covered by the severe winds although reduce their peak magnitude. Figure 22c gives the number of the grid-points of horizontal wind speed >17.2 m s^{-1} within the box encompassing the vortex (see the blue box in Fig. 22a). Also shown is the number of high-wind grid-points without the vortex. Clearly, the number of high-wind grids is almost halved when the low-level vortex is removed during 0600-0700 UTC. Later as the vortex weakened, its influence on the number of high-wind grid decreased as well.

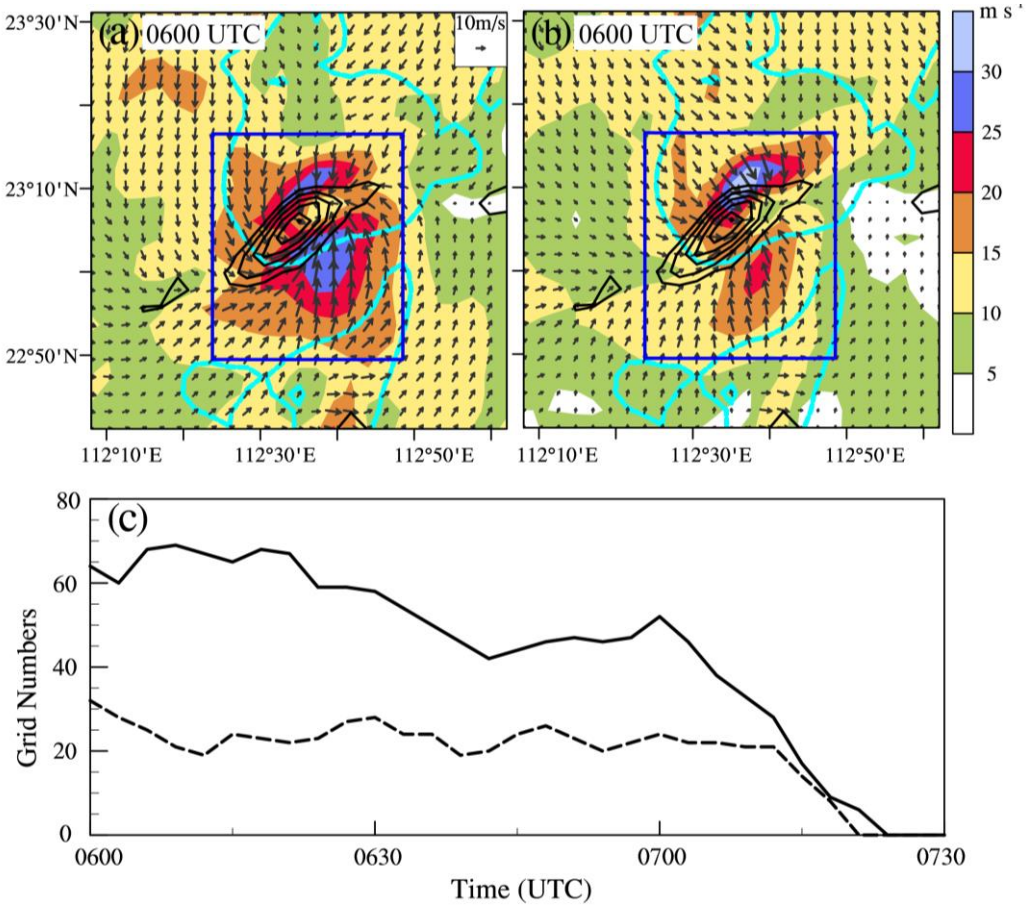

Fig. 22 (a) Simulated ground-relative winds (vectors) and speed (shading; unit: m s^{-1}) at 100 m AGL at 0600 UTC on 21 April 2017. (b) Same as (a) but with the effect of low-level vortex removed. Black contours denote positive vertical vorticity with an interval of 1×10^{-3} s^{-1}, while cyan ones are the 40-dBZ reflectivity. (c) Number of grid-points of horizontal wind speed >17.2 m s^{-1} in the region of high winds [see the blue boxes in (a) and (b)] with (black solid) and without (black dashed) the low-level vortex between 0600 and 0730 UTC.

Accepted for publication in *Journal of the Atmospheric Sciences*. DOI 10.1175/JAS-D-23-0047.1.

4. Summary and discussion

In this work, the dynamics of near-surface high winds produced by an unusually long-lived QLCS in South China on 21 April 2017 are investigated. Based upon the observation of operational radars and automatic weather stations, there were two episodes of high winds during the evolution of the QLCS. In the early stage, high winds mainly occurred at the apex of a small bow segment embedded in the southern QLCS. Later as the QLCS evolved into a large bow echo, much stronger high winds were produced at the system northern end where it merged with another MCS to the east.

A convection-permitting simulation was conducted using the WRF model to study the storm-scale thermal and dynamical processes responsible for the two episodes of high winds. In the early stage (Fig. 23a), the generation of high winds was ascribed to the local RIJ behind the apex of the small bowing segment, which occurred as gravity wave response to the thermal forcing in the leading convective line region. Initially, the RIJ was elevated above 2.0 km MSL, but it descended to the surface in response to the enhancement of low-level diabatic cooling which strengthened the downdrafts. Budget analyses of vertical momentum showed that the downdrafts at the leading edge of the RIJ were initiated by the negative buoyancy of cold pool and then strengthened by the weakened buoyancy-induced upward pressure gradient force in the boundary layer and enhanced hydrometeor loading above. High winds emerged near the bow apex as the descending RIJ transported high momentum to the surface.

The high winds in the merger stage formed in a manner distinctively different from that in the early stage (Fig. 23b). Backward trajectory tracking revealed that the high-wind parcels originated from low levels rather than descending from aloft with the RIJ. The superposition of ambient flow with the rotational flow of a low-level meso-β-scale vortex notably enhanced the area of high winds. This vortex was the northern one of the line-end vortices forming at the two ends of the bow echo. Initially, the line-end vortex was most evident at about 2.0 km MSL, with weak low-level rotation (Fig. 23a). When the northern part of the bow echo interacted with an intensifying large-scale shear line to its east, convection reorganization occurred owing to the large-scale convergence.

Accepted for publication in *Journal of the Atmospheric Sciences*. DOI 10.1175/JAS-D-23-0047.1.

Meanwhile, scattered convective cells developed along the shear line (Fig. 23a) which eventually evolved into a zonal convective line that merged with the northern bow echo. The merger greatly enhanced the low-level convergence which in turn increased the low-level rotation via vertical stretching of vertical vorticity.

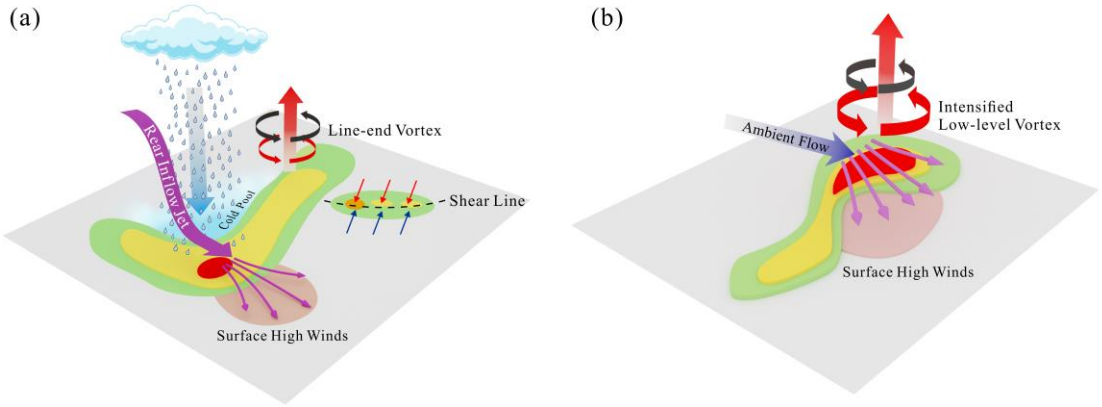

Fig. 23 Conceptual model for the generation of near-surface high winds in the (a) early and (b) merger stage of the QLCS.

This work focused on the storm-scale dynamics governing the generation of high winds, given the limit of 4-km model resolution. According to the observation of radar radial velocity, we also identified for this QLCS a number of meso-γ-scale vortices (i.e., MVs) which are capable of contributing to the high winds (e.g., Wakimoto et al. 2006; Atkins and Laurent 2009). The role of MVs will be further studied using subkilometer-scale simulations to more thoroughly understand the multiscale dynamics of high winds. Besides dynamical processes, microphysical processes also greatly affect the evolution of QLCSs and their high winds (e.g., Mahoney and Lackmann 2011; Adams-Selin et al. 2013; Zhou et al. 2020). In this work, the key microphysical processes controlling the intensity of the cold pool and downdrafts remain unclear which will be investigated according to polarimetric radar observation and numerical simulation in future research. Moreover, it should be noted that this work is a case study. Both the observational and idealized numerical studies of French and Parker (2012, 2014) showed considerable sensitivities of high winds to the environment conditions and the merger location. More QLCS cases in China will be examined to better understand the relationship between the merger and high winds.

The findings provide some useful insights into the operational forecast/warning of

Accepted for publication in *Journal of the Atmospheric Sciences*. DOI 10.1175/JAS-D-23-0047.1.

high winds caused by QLCSs. Merger of QLCS with another MCS can help prolong the convective system by convection reorganization in the merger region and produce even stronger high winds than by the RIJ. Thus, in addition to the bow-apex region, the merger region also deserves close monitoring which represents a location of potentially more damaging winds.

Acknowledgements. This work is mainly supported by the National Natural Science Foundation of China (grant no. 42122036, 42230607, 42105007), the Second Tibetan Plateau Scientific Expedition and Research (STEP) program (2019QZKK0105), and the open grants of State Key Laboratory of Severe Weather (2022LASW-B01). The authors are much grateful to the anonymous reviewers for their constructive comments and suggestions.

Data Availability Statement. The ERA5 reanalysis data can be downloaded from https://doi.org/10.24381/cds.bd0915c6. The atmospheric sounding data at Hongkong can be downloaded from http://weather.uwyo.edu/upperair/sounding.html. As for the severe weather reports and radar observations, please contact the corresponding author. The WRF model outputs have been uploaded to repository for archive (Ju 2023).

REFERENCES

Abulikemu, A., X. Xu, Y. Wang, J. Ding, and Y. Wang, 2015: Atypical occlusion process caused by merger of sea-breeze front and gust front. Adv. Atmos. Sci., **32**, 1431−1443, https://doi.org/10.1007/s00376-015-4260-2.

Abulikemu, A., Y. Wang, R. Gao, Y. Wang, and X. Xu, 2019: A numerical study of convection initiation associated with a gust front in Bohai Bay Region, North China. *J. Geophys. Res.*, **124**, 13843-13860, https://doi.org/10.1029/2019jd030883.

Adams-Selin, R. D., S. C. van den Heever, and R. H. Johnson, 2013: Impact of graupel parameterization schemes on idealized bow echo simulations. *Mon. Wea. Rev.*, **141**, 1241-1262, https://doi.org/10.1175/mwr-d-12-00064.1.

Adams, J. C., 1989: MUDPACK: Multigrid portable fortran software for the efficient solution of linear elliptic partial differential equations. *Appl. Math. Comput.*, **34**, 113-146, https://doi.org/https://doi.org/10.1016/0096-3003(89)90010-6.

Atkins, N. T., C. S. Bouchard, R. W. Przybylinski, R. J. Trapp, and G. Schmocker, 2005: Damaging surface wind mechanisms within the 10 June 2003 Saint Louis bow echo during BAMEX. *Mon. Wea. Rev.*, **133**, 2275-2296, https://doi.org/10.1175/mwr2973.1.

Atkins, N. T., and M. St. Laurent, 2009: Bow echo mesovortices. Part I: Processes that influence their damaging potential. *Mon. Wea. Rev.*, **137**, 1497-1513, https://doi.org/10.1175/2008mwr2649.1.

Brewster, K., M. Hu, M. Xue, and J. Gao, 2005: Efficient assimilation of radar data at high resolution for short-range numerical weather prediction. *Extended Abstract, WWRP Int. Symp. on Nowcasting and Very Short-range Forecasting*, Toulouse, France, WMO, 3.06, https://doi.org/http://twister.ou.edu/papers/BrewsterWWRP_Nowcasting.pdf.

Chen, X., X. Yu, and X. Wang, 2022: Investigation of derechos in China: Spatiotemporal distribution, environmental characteristics, and morphology of derechos producing convective systems. *Acta Meteorol. Sin.*, **80**, 67-81, https://doi.org/10.11676/qxxb2021.067.(in Chinese)

Coniglio, M. C., S. F. Corfidi, and J. S. Kain, 2011: Environment and early evolution of the 8 May 2009 derecho-producing convective system. *Mon. Wea. Rev.*, **139**, 1083-1102, https://doi.org/10.1175/2010mwr3413.1.

Davis, C., and Coauthors, 2004: The bow echo and MCV experiment: Observations and opportunities. *Bull. Amer. Meteor. Soc.*, **85**, 1075-1094, https://doi.org/10.1175/bams-85-8-1075.

Evans, C., M. L. Weisman, and L. F. Bosart, 2014: Development of an intense, warm-core mesoscale vortex associated with the 8 May 2009 “Super Derecho”

Accepted for publication in *Journal of the Atmospheric Sciences*. DOI 10.1175/JAS-D-23-0047.1.

convective event. *J. Atmos. Sci.*, **71**, 1218-1240, https://doi.org/10.1175/jas-d-13-0167.1.

Fovell, R. G., 2002: Upstream influence of numerically simulated squall-line storms. *Quart. J. Roy. Meteor. Soc*., **128**, 893–912, https://doi.org/https://doi.org/10.1256/0035900021643737.

French, A. J., and M. D. Parker, 2012: Observations of mergers between squall lines and isolated supercell thunderstorms. *Wea. Forecasting*, **27**, 255-278, https://doi.org/10.1175/waf-d-11-00058.1.

French, A. J., and M. D. Parker, 2014: Numerical simulations of bow echo formation following a squall line–supercell merger. *Mon. Wea. Rev.*, **142**, 4791-4822, https://doi.org/10.1175/mwr-d-13-00356.1.

Fujita, T. T., 1978: Manual of downburst identification for Project NIMROD. Satellite and Mesometeorology Research Paper 156, University of Chicago, 104pp.

Hersbach, H., and Coauthors, 2020: The ERA5 global reanalysis. *Quart. J. Roy. Meteor. Soc.*, **146**, 1999-2049, https://doi.org/https://doi.org/10.1002/qj.3803.

Houze, R. A., Jr., 2004: mesoscale convective systems. *Reviews of Geophysics*, **42**, RG4003, https://doi.org/https://doi.org/10.1029/2004RG000150.

Hua, S., X. Xu, and B. Chen, 2020: Influence of multiscale orography on the initiation and maintenance of a precipitating convective system in North China: A Case Study. *J. Geophys. Res.*, **125**, https://doi.org/10.1029/2019jd031731.

Iacono, M. J., J. S. Delamere, E. J. Mlawer, M. W. Shephard, S. A. Clough, and W. D. Collins, 2008: Radiative forcing by long-lived greenhouse gases: Calculations with the AER radiative transfer models. *J. Geophys. Res.*, **113**, https://doi.org/https://doi.org/10.1029/2008JD009944.

Janjić, Z. I., 1994: The Step-Mountain Eta Coordinate Model: Further Developments of the Convection, Viscous Sublayer, and Turbulence Closure Schemes. *Mon. Wea. Rev.*, **122**, 927-945, https://doi.org/10.1175/1520-0493(1994)122<0927:Tsmecm>2.0.Co;2.

Johns, R. H., and W. D. Hirt, 1987: Derechos: Widespread convectively induced windstorms. *Wea. Forecasting*, **2**, 32-49, https://doi.org/10.1175/1520-

Accepted for publication in *Journal of the Atmospheric Sciences*. DOI 10.1175/JAS-D-23-0047.1.

0434(1987)002<0032:Dwciw>2.0.Co;2.

Ju, Y., 2023: The Data for Two Episodes of High Winds in South China, Version 2. accessed 15 March 2023, https://doi.org/10.6084/m9.figshare.22093187.

Klimowski, B. A., M. R. Hjelmfelt, and M. J. Bunkers, 2004: Radar observations of the early evolution of bow echoes. *Wea. Forecasting*, **19**, 727-734, https://doi.org/10.1175/1520-0434(2004)019<0727:Rootee>2.0.Co;2.

Lafore, J.-P., and M. W. Moncrieff, 1989: A numerical investigation of the organization and interaction of the convective and stratiform regions of tropical squall lines. . *J. Atmos. Sci.*, **46**, 521-544, https://doi.org/10.1175/1520-0469(1989)046<0521:Anioto>2.0.Co;2.

Liu, Q., X. Xu, K. Zhao, and A. Zhou, 2023: A merger-formation bow echo caused by low-level mesovortex. *J. Geophys. Res. Atmos*., **128**, e2022JD037954, https://doi.org/10.1029/2022JD037954

Mahoney, K. M., and G. M. Lackmann, 2011: The sensitivity of momentum transport and severe surface winds to environmental moisture in idealized simulations of a mesoscale convective system. *Mon. Wea. Rev.*, **139**, 1352-1369, https://doi.org/10.1175/2010mwr3468.1.

Matsui, T., S. Q. Zhang, S. E. Lang, W.-K. Tao, C. Ichoku, and C. D. Peters-Lidard, 2020: Impact of radiation frequency, precipitation radiative forcing, and radiation column aggregation on convection-permitting West African monsoon simulations. *Clim. Dyn.*, **55**, 193-213, https://doi.org/10.1007/s00382-018-4187-2.

Meng, Z., D. Yan, and Y. Zhang, 2013: General features of squall lines in East China. *Mon. Wea. Rev.*, **141**, 1629-1647, https://doi.org/10.1175/mwr-d-12-00208.1.

Meng, Z., F. Zhang, P. Markowski, D. Wu, and K. Zhao, 2012: A modeling study on the development of a bowing structure and associated rear inflow within a squall line over South China. *J. Atmos. Sci.*, **69**, 1182-1207, https://doi.org/10.1175/jas-d-11-0121.1.

Parker, M. D., and R. H. Johnson, 2000: Organizational modes of midlatitude mesoscale convective systems. *Mon. Wea. Rev.*, **128**, 3413-3436, https://doi.org/10.1175/1520-0493(2001)129<3413:Omommc>2.0.Co;2.

Accepted for publication in *Journal of the Atmospheric Sciences*. DOI 10.1175/JAS-D-23-0047.1.

Pandya, R., and D. Durran, 1996: The influence of convectively generated thermal forcing on the mesoscale circulation around squall lines, *J. Atmos. Sci*., **53**, 2924–2951, https://doi.org/https://doi.org/10.1175/1520-0469(1996)053<2924:TIOCGT>2.0.CO;2.

Pandya, R., D. Durran, and M. L. Weisman, 2000: The influence of convective thermal forcing on the three-dimensional circulation around squall lines. *J. Atmos. Sci*., **57**, 29–45, https://doi.org/https://doi.org/10.1175/1520-0469(2000)057<0029:TIOCTF>2.0.CO;2.

Quan, W., X. Xu, and Y. Wang, 2014: Observation of a straight-line wind case caused by a gust front and its associated finer scale structures. *J. Meteor. Res*., **28**, 1137−1154, https://doi.org/10.1007/s13351-014-3080-0

Skamarock, C., and Coauthors, 2019: A description of the Advanced Research WRF Model Version 4.1. NCAR Tech. No. NCAR/TN-556+STR, https://doi.org/10.5065/1dfh-6p97.

Skamarock, W. C., M. L. Weisman, and J. B. Klemp, 1994: Three-dimensional evolution of simulated long-lived squall lines. *J. Atmos. Sci.*, **51**, 2563-2584, https://doi.org/10.1175/1520-0469(1994)051<2563:Tdeosl>2.0.Co;2.

Smull, B. F., and R. A. Houze, 1987: Rear inflow in squall lines with trailing stratiform precipitation. *Mon. Wea. Rev.*, **115**, 2869-2889, https://doi.org/10.1175/1520-0493(1987)115<2869:Riislw>2.0.Co;2.

Sun, H., Y. Luo, R. Zhang, L. Liu, and G. Wang, 2011: Analysis on the mature-stage features of the severe squall line occurring over the Yellow River and Huaihe River basins during 3-4 June 2009. *Chinese J. Atmos. Sci.*, **35**, 105-120, https://doi.org/10.3878/j.issn.1006-9895.2011.01.09.(in Chinese)

Sun, J., and N. A. Crook, 2001: Real-time low-level wind and temperature analysis using single WSR-88D data. *Wea. Forecasting*, **16**, 117-132, https://doi.org/10.1175/1520-0434(2001)016<0117:Rtllwa>2.0.Co;2.

Tang, Y., X. Xu, M. Xue, J. p. Tang, and Y. Wang, 2020: Characteristics of low-level meso-γ-scale vortices in the warm season over East China. *Atmos. Res.*, **235**, https://doi.org/10.1016/j.atmosres.2019.104768.

Accepted for publication in *Journal of the Atmospheric Sciences*. DOI 10.1175/JAS-D-23-0047.1.

Tang, Y., X. Xu, Y. Ju, Z. Wu, S. Zhang, X. Chen, and Q. Xu, 2023: Statistical analysis of mesovortices during the first rainy season in Guangdong, South China. *Remote Sensing*, **15**(8), 2176, https://doi.org/10.3390/rs15082176

Tewari, M., and Coauthors, 2004: Implementation and verification of the unified Noah land-surface model in the WRF model. *20th Conf. on Weather Analysis and Forecasting/16th Conf. on Numerical Weather Prediction*, Seattle, WA, US, American Meteorological Society, 17.15, https://doi.org/http://ams.confex.com/ams/84Annual/techprogram/paper_69061.htm.

Thompson, G., P. R. Field, R. M. Rasmussen, and W. D. Hall, 2008: Explicit forecasts of winter precipitation using an improved bulk microphysics scheme. Part II: Implementation of a new snow parameterization. *Mon. Wea. Rev.*, **136**, 5095-5115, https://doi.org/10.1175/2008mwr2387.1.

Wakimoto, R. M., H. V. Murphey, C. A. Davis, and N. T. Atkins, 2006: High winds generated by bow echoes. Part II: The relationship between the mesovortices and damaging straight-line winds. *Mon. Wea. Rev.*, **134**, 2813-2829, https://doi.org/10.1175/mwr3216.1.

Wei, P., and Coauthors, 2022: On the key dynamical processes supporting the 21.7 Zhengzhou record-breaking hourly rainfall in China. *Adv. Atmos. Sci.*, **40**, 337-349, https://doi.org/10.1007/s00376-022-2061-y.

Weisman, M. L., 1992: The role of convectively generated rear-inflow jets in the evolution of long-lived mesoconvective systems. *J. Atmos. Sci.*, **49**, 1826-1847, https://doi.org/10.1175/1520-0469(1992)049<1826:Trocgr>2.0.Co;2.

Weisman, M. L., 2001: Bow echoes: A tribute to T. T. Fujita. *Bull. Amer. Meteor. Soc.*, **82**, 97-116, https://doi.org/10.1175/1520-0477(2001)082<0097:Beattt>2.3.Co;2.

Weisman, M. L., and C. A. Davis, 1998: Mechanisms for the generation of mesoscale vortices within quasi-linear convective systems. *J. Atmos. Sci.*, **55**, 2603-2622, https://doi.org/10.1175/1520-0469(1998)055<2603:Mftgom>2.0.Co;2.

Weisman, M. L., and R. J. Trapp, 2003: Low-level mesovortices within squall lines and bow echoes. Part I: Overview and dependence on environmental shear. *Mon. Wea.*

Accepted for publication in *Journal of the Atmospheric Sciences*. DOI 10.1175/JAS-D-23-0047.1.

Rev., **131**, 2779-2803, https://doi.org/10.1175/1520-0493(2003)131<2779:Lmwsla>2.0.Co;2.

Wheatley, D. M., R. J. Trapp, and N. T. Atkins, 2006: Radar and damage analysis of severe bow echoes observed during BAMEX. *Mon. Wea. Rev.*, **134**, 791-806, https://doi.org/10.1175/mwr3100.1.

Wu, G., and Coauthors, 2015: Tibetan Plateau climate dynamics: Recent research progress and outlook. *Natl. Sci. Rev.*, **2**, 100-116, https://doi.org/https://doi.org/10.1093/nsr/nwu045.

Xia, R., D. Wang, J. Sun, G. Wang, and G. Xia, 2012: An observational analysis of a derecho in South China. *Acta Meteorol. Sin.*, **26**, 773-787, https://doi.org/10.1007/s13351-012-0608-z.

Xu, X., M. Xue, and Y. Wang, 2015a: The genesis of mesovortices within a real-data simulation of a bow echo system. *J. Atmos. Sci.*, **72**, 1963-1986, https://doi.org/10.1175/jas-d-14-0209.1.

Xu, X., M. Xue, and Y. Wang, 2015b: Mesovortices within the 8 May 2009 bow echo over the Central United States: Analyses of the characteristics and evolution based on Doppler radar observations and a high-resolution model simulation. *Mon. Wea. Rev.*, **143**, 2266-2290, https://doi.org/10.1175/mwr-d-14-00234.1.

Xu, X., M. Xue, Y. Wang, and H. Huang, 2017: Mechanisms of secondary convection within a Mei-Yu frontal mesoscale convective system in eastern China. *J. Geophys. Res.*, **122**, 47-64, https://doi.org/10.1002/2016jd026017.

Xue, C., X. Shen, Z. Ding, N. Wu, Y. Zhang, X. Chen, and C. Guo, 2022: Organizational modes of spring and summer convective storms and associated severe weather over southern China during 2015–19. *Mon. Wea. Rev.*, **150**, 3031-3049, https://doi.org/10.1175/mwr-d-22-0061.1.

Xue, M., and Coauthors, 2000: The Advanced Regional Prediction System (ARPS) – A multi-scale nonhydrostatic atmospheric simulation and prediction tool. Part II: Model physics and applications. *Meteorol. Atmos. Phys.*, **76**, 143-165, https://doi.org/10.1007/s007030170027.

Yang, M.-H., and R. A. Houze, 1995: Sensitivity of squall-line rear inflow to ice

Accepted for publication in *Journal of the Atmospheric Sciences*. DOI 10.1175/JAS-D-23-0047.1.

microphysics and environmental humidity. *Mon. Wea. Rev.*, **123**, 3175-3193, https://doi.org/10.1175/1520-0493(1995)123<3175:Soslri>2.0.Co;2.

Yang, X., J. Sun, and Y. Zheng, 2017: A 5-yr climatology of severe convective wind events over China. *Wea. Forecasting*, **32**, 1289-1299, https://doi.org/10.1175/waf-d-16-0101.1.

Yao, Y., X. Yu, Y. Zhang, H. Cheng, M. Wei, and J. Li, 2008: Analysis on a typical squall line case with Doppler weather radar data. *Plateau Meteorol.*, **27**, 373-381.

Zhang, D.-L., and K. Gao, 1989: Numerical simulation of an intense squall line during 10–11 June 1985 pre-storm. Part II: Rear inflow, surface pressure perturbations and stratiform precipitation. *Mon. Wea. Rev.*, **117**, 2067-2094, https://doi.org/10.1175/1520-0493(1989)117<2067:Nsoais>2.0.Co;2.

Zhang, L., J. Sun, Z. Ying, and X. Xiao, 2021: Initiation and development of a squall line crossing Hangzhou Bay. *J. Geophys. Res.*, **126**, e2020JD032504, https://doi.org/https://doi.org/10.1029/2020JD032504.

Zhang, S., and Coauthors, 2023: Dynamics governing a simulated bow-and-arrow-type mesoscale convective system. *Mon. Wea. Rev.*, **151**, 603-623, https://doi.org/10.1175/mwr-d-22-0091.1.

Zhou, A., K. Zhao, W. C. Lee, H. Huang, D. Hu, and P. Fu, 2020: VDRAS and polarimetric radar investigation of a bow echo formation after a squall line merged with a preline convective cell. *J. Geophys. Res.*, **125**, https://doi.org/10.1029/2019jd031719.

Zhou, A., K. Zhao, X. Xu, Q. Liu, Z. Ding, H. Huang, X. Liu, X. Rao, and S. Hu, 2023: A climatological study on the two types of bow echoes over South China. *J. Geophy. Res.*, **128**, e2023JD038720. https://doi.org/10.1029/2023JD038720.

Accepted for publication in *Journal of the Atmospheric Sciences*. DOI 10.1175/JAS-D-23-0047.1.